



ORIGINAL ARTICLE

Contributions of arid climate and hydrothermal fluid flow on sedimentation in saline-alkaline lakes: Insight from the Ibar intramontane basin (Southern Serbia)

Nevena Andrić-Tomašević¹  | Benjamin F. Walter^{2,3,4} | Vladimir Simić⁵ | Mohsin Raza^{2,3} | Dragana Životić⁵  | Željana Novković⁶ | Jochen Kolb^{2,3} | Axel Gerdes^{7,8} | Aratz Beranoaguirre^{2,3,7,8}

¹Institute of Applied Geosciences, Karlsruhe Institute of Technology (KIT), Karlsruhe, Germany

²Economic Geology and Geochemistry, Karlsruhe Institute of Technology (KIT), Karlsruhe, Germany

³Laboratory for Environmental and Raw Material Analyses (LERA), Karlsruhe Institute of Technology (KIT), Karlsruhe, Germany

⁴Department of Geosciences, Petrology and Mineral Resources, University of Tuebingen, Tübingen, Germany

⁵Faculty of Mining and Geology, University of Belgrade, Belgrade, Serbia

⁶MMI Bor Mining and Metallurgy, Bor, Serbia

⁷Institut für Geowissenschaften, Goethe-Universität Frankfurt, Frankfurt am Main, Germany

⁸Frankfurt Isotope and Element Research Center (FIERCE), Goethe-Universität Frankfurt, Frankfurt am Main, Germany

Correspondence

Nevena Andrić-Tomašević, Institute of Applied Geosciences, Karlsruhe Institute of Technology (KIT), Adenauerring 20b, Karlsruhe 76131, Germany.
Email: nevena.tomasevic@kit.edu

Funding information

Ministry of Science, Technological Development and Innovation, Republic

Abstract

Saline-alkaline lakes are common in tectonically active, semi-arid regions, resulting from the interplay between tectonic, hydrothermal, surface processes and climate. This study investigates their contribution to the evolution of the saline-alkaline succession in the intramontane Ibar Basin (Southern Serbia). The succession is investigated using detailed sedimentological analysis, in situ U–Pb geochronology of carbonates acquired by laser ablation inductively coupled plasma mass spectrometry (LA-ICP-MS), major and trace element geochemistry and fluid inclusion analysis. Dominantly clastic sedimentation is represented by alluvial fan, flood plain, delta and marginal and profundal lake facies associations. Microbialite and littoral to sublittoral oil shales formed in the areas protected from clastic input. The stratigraphic succession shows a transition from alluvia to a hydrologically open and closed lacustrine environment. U–Pb geochronology of microbialite of a close lake phase (~17 Ma) suggests basin evolution during the Early to Middle Miocene age. The hydrologically closed lake phase is marked by borate-rich facies, which comprise mainly colemanite overgrown by secondary ulexite within profundal lake facies associations. The textural features suggest that colemanite initially precipitated at or below the sediment/water interface. The subsequent growth, as observed from the primary fluid inclusions in colemanite and calcite, indicates precipitation from the evolving bittern brine under evaporitic, redox conditions, which during diagenesis reached temperatures of 200–220°C. High $\text{Ca}^{2+}/\text{Na}^{+}$ ratios in the brine favour colemanite precipitation. Gradual Ca^{2+} depletion and clay breakdown (dewatering) lead to ulexite and borax precipitates. The results imply that B, Ca and Na were mobilised and transported into the basin by hydrothermal fluids that previously leached bedrock and/or by streams carrying products of the volcanic rocks' weathering. However, brine saturation and syndepositional precipitation were initiated by an

This is an open access article under the terms of the [Creative Commons Attribution](https://creativecommons.org/licenses/by/4.0/) License, which permits use, distribution and reproduction in any medium, provided the original work is properly cited.

© 2025 The Author(s). *The Depositional Record* published by John Wiley & Sons Ltd on behalf of International Association of Sedimentologists.

of Serbia, Grant/Award Number: 451-03-47/2023-01/200126 and 451-03-66/2024-03/200052; Deutsche Forschungsgemeinschaft, Grant/Award Number: INST 121384/213-1 FUGG and TO 1364 3-1

arid climate through evaporation, while further growth was driven by reflux of fluids during diagenesis. This study highlights the importance of the tectonics of the collisional orogens and associated processes, arid climate and basin hydrological regime on the deposition of B, Ca-rich deposits in saline-alkaline lakes.

KEYWORDS

borate, climate, Dinarides, hydrothermal, Miocene, saline-alkaline lakes, tectonics

1 | INTRODUCTION

Intramontane basins in arid to semi-arid regions commonly have heterogeneous depositional successions varying over multiple temporal and spatial scales. The complexity of the system results from several factors such as precipitation rates, evaporation, weathering of the basement rocks, groundwater, biological activity, drainage basin and hydrology governed by the interplay between climate and tectonics (e.g. Carroll & Bohacs, 1999; Cohen et al., 2015; Deocampo & Jones, 2014; Pietras & Carroll, 2006). During their evolution, intramontane basins may become hydrologically closed and show saline-alkaline character (e.g. Obradović et al., 1997; Pietras et al., 2003; Renaut et al., 2021; Smith, 1979). The hydrology of many tectonically active intramontane basins includes the contribution of hot springs (e.g. Eugster & Jones, 1968; De Filipis et al., 2013; Andrić-Tomašević et al., 2024). However, their control over the deposition may be unnoticed in ancient basins, where direct evidence of hot springs discharging into the basin may be missing due to the scarcity of sedimentary records or diagenetic effects (e.g. Lowenstein et al., 2017; Lowenstein & Lauren, 2016). Subsequently, this may lead to false ideas about palaeoclimatic and palaeoenvironmental conditions in which the basins developed and their contribution to basin sedimentation.

The goal of this work was to assess the effect of geothermal fluids on the deposition in the Early to Middle Miocene Piskanja deposit, Ibar Basin, Southern Serbia (Figure 1). Numerous intramontane basins formed during the Oligocene–Miocene post-collisional evolutionary stage of the Dinarides (Figure 1). Deposition in many of these basins was affected by extensional tectonic events being active during the Early to Middle Miocene (e.g. Andrić, Sant, et al., 2017; Andrić-Tomašević et al., 2024; Matenco & Radivojević, 2012). In addition, their evolution (~18–13 Ma, de Leeuw et al., 2011; Mandić et al., 2009; Sant, Mandić, et al., 2018; Sant, Andrić, et al., 2018) overlaps with the Miocene Climatic Optimum (MCO, Zachos et al., 2001), which probably significantly contributed to their evolution. The presence of sedimentary successions rich in evaporitic minerals in numerous basins (e.g. Ibar Basin, Obradović et al., 1992; Pranjani Basin,

Andrić-Tomašević et al., 2021; Valjevo-Mionica Basin, Šajnović et al., 2008; Lopare Basin, Šajnović et al., 2020) located in the internal Dinarides implies dry climatic conditions despite the globally humid climate during the MCO. Interestingly, many of these basins (e.g. Ibar Basin, Kraljevo-Čačak Basin, Valjevo-Mionica Basin) are spatially linked to Tertiary magmatic regions (e.g. Cvetković et al., 2013) and are likely recharged by hot springs at some stage of their evolution. In such a situation, mineralised waters from hot springs may significantly contribute to the lacustrine water's high alkalinity (e.g. Eugster & Jones, 1968; Lowenstein et al., 2017; Renaut et al., 2021).

For two reasons, the optimal place to study the interplay between climate and hot springs on the deposition of the intramontane basins (Figure 1) is the Miocene Ibar Basin, located in the Dinarides, Southeast (SE) Europe. Firstly, the basin was situated in the internal Dinarides, probably affected by an arid climate during its evolution. Secondly, the basin developed in the extensional regime affecting the region dominated by Oligocene–Miocene magmatic rocks (e.g. Andrić et al., 2015; Mladenović et al., 2015; Schefer et al., 2011). The study focuses on the Piskanja sedimentary succession of the Ibar Basin. The objectives include (1) sedimentological analysis of the sediments deposited in the Piskanja sedimentary succession; (2) mineralogical and geochemical characterisation of boron minerals; (3) tracing the brine source and its temperature through hot spring evolution; (4) delineating the mechanisms controlling the deposition in the Piskanja sedimentary succession; (5) disentangling the role of the hot springs and arid climatic conditions in sedimentation in the Ibar saline-alkaline lake during the Miocene. To reach the study objectives, we employ an *in situ* calcite U–Pb geochronology approach in combination with petrographic, mineralogical, sedimentological and fluid inclusion analysis to reconstruct the depositional evolution in space and time.

These new data will provide insight into the impact and roles of climate and hydrothermal fluid flow on the development and nature of the depositional sequences in lacustrine intramontane basins in collisional systems. New U–Pb age data have important implications for the definition of timing and modalities of climatic variations

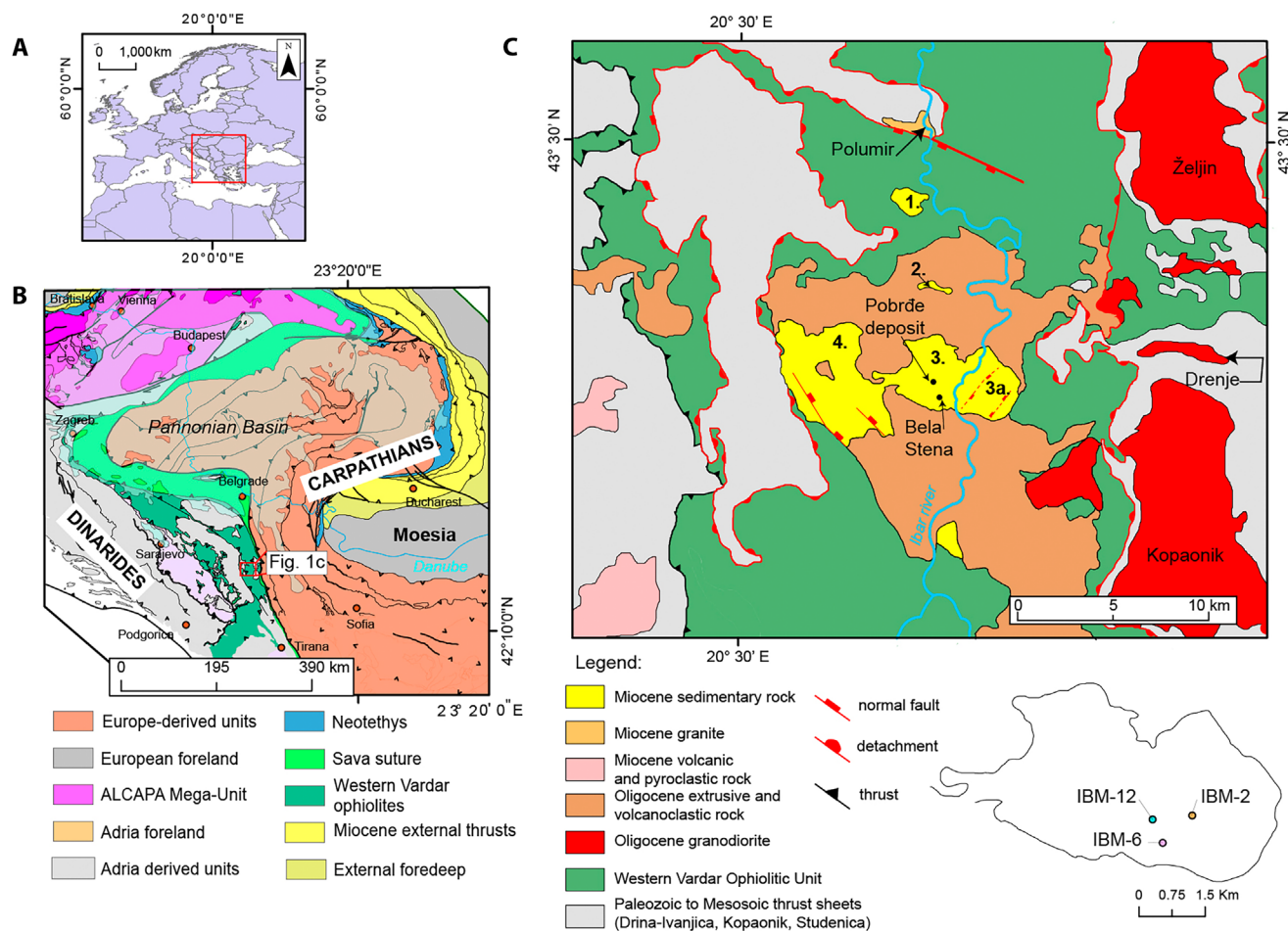


FIGURE 1 (A) Simplified map of Europe with the location of the Alpine–Carpathian–Dinaridic system. (B) Tectonic map of Alpine–Carpathian–Dinaridic system (modified after Schmid et al., 2008). The red rectangle delineates the extent of (C). (C) Geological map of the study area (after Schefer et al., 2011); Basic Geological Map of Serbia, 1: 100,000; Sheets Novi Pazar (Urošević et al., 1970a), Vrnjci (Urošević et al., 1970b), Sjenica (Mojsilović et al., 1978) and Ivanjica Brković et al. (1976) with the inset showing the eastern part of Ibar Basin, also known as Piskanja sedimentary succession, and the location of the boreholes from which samples were taken. Yellow polygons resemble present-day remains of the Ibar Basin.

in south-eastern Europe during the MCO. Furthermore, they will serve to highlight the ability of orogens with small topography, such as the Dinarides, to modulate global climatic conditions, such as the MCO, locally.

2 | GEOLOGICAL SETTING

The Miocene intermontane Ibar Basin is situated in the south-eastern part of the Dinarides mountain belt (southern Serbia, Figure 1). The basin is formed above a Late Cretaceous to Eocene, Adria-derived nappe stack, which developed in the context of the Adria–Europe collision (Schmid et al., 2008). Ophiolite obduction onto the distal Adriatic continental margin during the Late Jurassic and subsequent closure of the last Neotethys oceanic realm, forming the Sava suture zone, predates the collision (Pamić et al., 2002; Schmid et al., 2008). During

the late Cretaceous–Eocene mountain-building process in the Dinarides, the ophiolites were affected by out-of-sequence thrusting. This process leads to the formation of composite nappes, the Adria-derived continental units in the lower part of the tectonic stack and the ophiolites in the upper (Dimitrijević, 1997; Schmid et al., 2008). The composite Drina–Ivanjica and Jadar–Kopaonik–Studenica thrust sheets comprise non-metamorphosed to slightly metamorphosed Upper Palaeozoic–Lower Jurassic sedimentary rocks of the distal Adria margin, which are tectonically overthrust by Late Jurassic ophiolites (Figure 1, Dimitrijević, 1997; Karamata, 2006; Schmid et al., 2008; Schefer et al., 2010). The Jadar–Kopaonik–Studenica thrust sheet east of the Ibar Valley (Figure 1) is intruded by the Late Oligocene Željina, Drenje (31.7–31.2 Ma, Schefer et al., 2011) and Kopaonik (30.9–30.7 Ma, Schefer et al., 2011) massifs of granodiorite composition. This is associated with dacitic-andesitic volcanic and

volcanoclastic rocks (31 Ma—Cvetković et al., 1995) that cover the ophiolites discordantly (Cvetković et al., 1995; Schefer et al., 2011). Subsequently, this was followed by quartz-latite and quartz monzonite, mostly present in the south-eastern part of the study area (Figure 1) and further to the south (including also the Rogozna Mt. magmatic complex further to the southwest, ~29–27 Ma, Borojević-Šoštarić et al., 2012). These magmatic episodes are associated with a pronounced late magmatic-hydrothermal activity (e.g. Cvetković et al., 1995; Karamata et al., 1994).

During the Miocene, the Dinarides began experiencing extension (e.g. Andrić, Sant, et al., 2017; Ilić & Neubauer, 2005) at low rates in the Late Oligocene–Early Miocene (Erak et al., 2017), reaching its peak around 14–15 Ma (Stojadinović et al., 2013). The extension is probably controlled by (1) west to southwestward retreat and subsequent break-off of the Dinaridic slab (e.g. Andrić, Vogt, et al., 2018; Matenco & Radivojević, 2012) and (2) the northeastward retreat of the Carpathian slab (Fodor et al., 2005). In the study area, this extensional phase led to Early Miocene North–South (N–S) and Middle Miocene East–West (E–W)-directed extensional events (Schefer et al., 2011). The older, N–S-directed extensional event drove the exhumation of the Studenica and Kopaonik core complexes starting at ~21–17 Ma (based on $^{40}\text{Ar}/^{39}\text{Ar}$ biotite ages; Schefer et al., 2010). The uplift ended at ~10 Ma (apatite and fission track data, AFT and ZFT, respectively, Schefer et al., 2011). The whole tectonic omission is assumed to reach ~10 km in thickness (Schefer et al., 2010). The core-complex formation was associated with intrusion and exhumation of the Golija granite (20.6–20.2 Ma) and the syn-kinematic S-type Polumir granite (18.1–17.4 Ma). Moreover, this process drove the exhumation of the older Oligocene I-type granitic rocks of Kopaonik and Drenje

(Schefer et al., 2011). The Miocene volcanism forms lava flows and pyroclastic rocks of quartz-latitic composition (Cvetković, 2002; Cvetković & Pécskay, 1999).

2.1 | Stratigraphy of the Ibar Basin

The Ibar Basin was part of the Neogene Serbian lake system that occupied depressions mainly located in the internal Dinarides during Oligocene–Miocene times (e.g. Krstić et al., 2001, 2003; Obradović & Vasić, 2007). Most of these lakes formed between ~18 and 13 Ma (de Leeuw et al., 2011, 2012; Sant, Mandić, et al., 2018; Sant, Andrić, et al., 2018), overlapping with the MCO (Zachos et al., 2001). In many of them, the deposition was coeval with extension, suggesting a significant contribution of the tectonics to their development (e.g. Andrić, Sant, et al., 2017; Andrić-Tomašević et al., 2021, 2024). The Ibar Basin formed in the hanging wall of the low-angle detachment fault along which the Studenica metamorphic dome is exhumed (Andrić et al., 2015; Schefer et al., 2011). Today, the Ibar Basin includes four subbasins, Tadenje, Ušće, Jarando and Gradac (Figure 1C, Ercegovac et al., 1991). The samples analysed in this study originate from the Piskanja sedimentary succession located in the south-eastern part of the Jarando sub-basin (inset on Figure 1C).

The sedimentary record starts with the deposition of alluvial, breccio-conglomerate, sandstone and marlstone intercalated with several bituminous coal seams (Figure 2, Anđelković et al., 1991; Ercegovac et al., 1991). The coal seams were superimposed by laminated, dolomitic marlstone and claystone, alternating with sandstone and conglomerate, of a lacustrine to playa depositional environment (e.g. Gagic, 1985; Obradović, 1983;

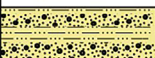

Age	Lithology	Thickness (m)	Description
Pliocene		150	Conglomerate, sandstone, claystone, marly limestone, gravel, sand and clay
Miocene		1000	<div>Massive carbonates</div> <div>Boron mineralisation zones</div> <div>Sandstone, clay, marlstone, marly limestone and conglomerate</div> <div>Magnesite lenses</div> <div>Coal series, conglomerate, marlstone, sandstone, claystone and tuff</div> <div>Conglomerate, sandstone interbedded with volcanoclastite</div>

FIGURE 2 General stratigraphic column of the Ibar Basin (modified by Andrić et al., 2015; Brković et al., 1976; Mojsilović et al., 1978; Urošević et al., 1970a, 1970b).

Obradović & Vasić, 2007). The maximum thickness of the sediments in the Ibar Basin reaches ~1500 m (based on geophysical exploration, Anđelković et al., 1991). Because there are no precise geochronological data for a sedimentary succession of the Ibar Basin, the age of the main depositional phases is inferred by comparing the fossil material with remains from other nearby basins in the Serbian Lake System. The alluvial deposition in the Ibar Basin started at ~19–17 Ma (Andrić et al., 2015; Krstić et al., 2001; Prysazhnjuk et al., 2000), which also correlates with the onset of extension (Schefer et al., 2011). The dominant lacustrine phase started at ~16–15 Ma (Kochansky & Slisković, 1981).

The basin contains bituminous coal (Ercegovac et al., 1991), magnesite (Bela Stena locality, Falick et al., 1991) and stratigraphically higher, widespread borate and borosilicate mineralisation (Obradović et al., 1992) alternating with microbialites (marked as a travertine in Andrić et al., 2015). The maturity of the Cenozoic coals is influenced by elevated heat flow associated with magmatism (Ercegovac et al., 1991) and exhumation of the metamorphic core complexes of Studenica and Kopaonik (Andrić et al., 2015). The magnesite occurs as beds and lenses (Figure 2), often accompanied by dolomite. Falick et al. (1991) suggest that the Mg^{2+} was carried by hydrothermal fluids and surface waters flowing over a nearby ophiolitic terrain, a surrounding palaeorelief.

Previous studies document colemanite ($Ca_2B_6O_{11} \cdot 5H_2O$, Jackson Jr., 1884) as the most common borate and howlite ($Ca_2B_5SiO_9(OH)_5$, How, 1868) as the most common borosilicate in the Pobrđe deposit, northwest of the Jarando subbasin (Figure 1C,E, e.g. Obradović et al., 1992). The occurrence of B-rich deposits within the basin is assumed to be confined by faults (Obradović et al., 1992). Colemanite is mainly brecciated and recrystallised with euhedral grains reaching a few centimetre in size, filling fractures within the claystone-rich layers. It may alternate with dark grey claystone and chert. Howlite forms fine-grained milky to white aggregates, nodular masses or wormlike bodies within clay-rich groundmass. It forms along the colemanite. The B-rich beds may reach up to 2.5 m in thickness. Occasionally, borate and borosilicate aggregates may contain hydrocarbons. Other boron minerals, such as searlesite ($NaBSi_2O_5(OH)_2$, Larsen & Hicks, 1914) and lüneburgite ($Mg_3[B_2(OH)_6](PO_4)_2 \cdot 6H_2O$, Nöllner, 1870), occur in traces as secondary fissure fillings. Obradović et al. (1992) suggested hydrothermal fluid flow associated with the magmatism as an important source of B, Ca and Na.

The vitrinite reflectance and the detrital apatite fission track data recorded by the sedimentary rocks from the Jarando and Tadenje subbasins show post-depositional thermal overprint between 17 Ma and 10–8 Ma, reaching maximum burial temperatures of 100–130°C

(Andrić et al., 2015). This thermal event is correlated with the exhumation of core complexes of the Jadar-Kopaonik-Studenica composite thrust sheets. The subsequent cooling episode is attributed to basin inversion and erosion. However, Andrić et al. (2015) linked local thermal disturbances in the SE of the Ibar Basin (Piskanja sedimentary succession, at ~7.1 Ma) to the most recent hydrothermal phase. This phase is associated with Serbia's youngest high-K calc-alkaline to shoshonite and ultrapotassic magmatic event (Cvetković et al., 2004).

3 | METHODS

3.1 | Sedimentological analysis and sampling strategy

A detailed sedimentological analysis has been done on the boreholes IBM-2, IBM-6 and IBM-12 located in the Piskanja sedimentary succession, Ibar Basin (Figures 1, 3–6). This allowed the distinction of 23 facies based on lithology, texture, structure, contact with underlying and overlying units, and colour (Table 1, e.g. Cohen et al., 1997; García-García et al., 2006; Miall, 1996). Facies associations are defined by grouping particular facies based on the vertical association of distinguished facies. Subsequently, 9 facies associations are observed in alluvial, deltaic, shallow and deep lacustrine depositional systems.

3.2 | Geochemistry

The contents of major oxides in 40 shale samples from borehole IBM-2 were determined by X-ray fluorescence (XRF) analysis in the Laboratory at MMI Bor Mining and Metallurgy (Bor, Serbia). Selected trace elements from the same samples were determined by inductively coupled plasma-mass spectrometry (ICP-MS). XRF analysis was conducted on RIGAKU Super Mini 200 XRF analyser. Dried samples were heated at 1000°C, and after cooling, 2.5 g of each sample with 6 g of solvent (made of Li-tetraborate and Li-metaborate, 3:1) were homogenised and furnace. Trace elements were analysed by ICP-MS on Agilent 7700 following the procedures outlined by ASTM D6357-21a (2021) standard. For digestion, 0.2–0.5 g of powdered (<150 µm) sample was placed into a 100 or 200 mg Teflon beaker and 20 mL of aqua regia and 20 mL of concentrated HCl were added to the beaker. After that, the beaker was heated to 130–150°C; after the solution evaporated, the beaker was removed and cooled to room temperature. After cooling, 1 mL of concentrated HNO_3 and 20 mL of H_2O were added to the beaker and heated at 90–100°C. The solution was cooled to room temperature

and diluted with water. The content of major and minor elements is presented in [Tables S1](#) and [S2](#), and [Figure 7](#).

3.3 | U–Pb geochronology

A sample of authigenic microbialite (Ibar 7ab, borehole IBM-2, depth 78.5–78.6 m, [Figures 1, 3](#) and [8](#)) and cavity-filling calcite were dated by U–Pb in two independent sessions using a ThermoFisher Scientific Element XR sector-field single-collector ICP-MS coupled to a 193-nm ArF Excimer laser with a HelEx 2-volume cell (Analyte Excite+, Teledyne PhotonMachines) at the Laboratory for Environmental and Raw Materials Analysis (LERA), Karlsruhe Institute of Technology (Germany). Due to the low U and Pb concentrations in cavity-filling calcite, it was analysed in an additional third session at FIERCE (Frankfurt Isotope & Element Research Center, Goethe University Frankfurt, Germany) using a RESOLUTION 193 nm ArF excimer laser coupled to a ThermoFisher Scientific Neptune Plus multicollector ICP-MS. The methodology for both instruments was modified after Beranoaguirre et al. (2022) and is detailed in supplementary data tables (including spot size, acquisition time or reference material information/results). SRMNIST612 and SRMNIST614 (Jochum et al., 2011) were analysed repeatedly to correct for mass bias, interelement fractionation and instrumental drift during each. Carbonate reference material WC1 (Roberts et al., 2017), JT-1 (Guillong et al., 2020), B-6 (only LA-ICP-MS data, Pagel et al., 2018), ASH15D (Nuriel et al., 2021) and Duff Brown Tank (Hill et al., 2016) were used as carbonate matrix-matched reference materials. Raw data were corrected offline using an in-house VBA spreadsheet program (Gerdes & Zeh, 2006, 2009), and ages were calculated as lower Concordia-curve intercepts using the same algorithms as ISOPLOT 4.15 (Ludwig, 2012). Data are presented in [Table S3](#).

3.4 | Petrographic analysis (polarisation microscopy, SEM and cathodoluminescence imaging)

Petrographic analysis of the six borehole samples IBM-2 (Ibar 1, 209–210.6 m; Ibar 2, 210.6–211.3 m; Ibar 3, 211.1–212.1 m and Ibar 4, 212.6–213 m, [Figures 1](#) and [3](#)), IBM-6 (Ibar 5, 140.7–141.2 m, [Figures 1](#) and [4](#)) and IBM-12 (Ibar 6, 428.2–429.1 m, [Figures 1](#) and [5](#)) used for fluid-inclusion analysis were made using a polarised microscope and SEM. All thin sections were studied by light microscopy and scanning electron microscopy (Phenom XL, Thermo Fisher Scientific) at the Department of Geosciences, University of Tübingen at 15 kV. To

constrain textural information of fluid inclusion assemblages (FIAs), CL microscopy of different host phases (B-minerals and calcite) was done (e.g. Epp et al., 2019; Kolchugin et al., 2016, 2020; Kreissl et al., 2018; Müller et al., 2020; Müller, Jacquemyn, et al., 2022; Müller, Walter, et al., 2022). A ‘hot cathode’ CL microscope (type HC1-LM) at the University of Tübingen was used with an acceleration voltage of the electron beam ~14 kV and a beam current density of ~9–2 μAmm on the sample surface.

3.5 | Fluid inclusion analysis

The same six samples have been analysed for fluid inclusions. CL microscopy of calcite and colemanite was applied to shed light on ‘hidden’ textures. This is a prerequisite to correctly determine the fluid petrography and timing of FIAs (e.g. Epp et al., 2019; Keim et al., 2019; Kolchugin et al., 2016, 2020; Kreissl et al., 2018; Müller, Jacquemyn, et al., 2022; Müller, Walter, et al., 2022; Müller, Jacquemyn, et al., 2022; Müller, Walter, et al., 2022; Walter et al., 2015, 2018, 2023). A ‘hot cathode’ CL device (type HC1-LM) at the University of Tübingen was used with an acceleration voltage of the electron beam ~14 kV and a beam current density of ~9–2 μAmm on the sample surface.

Microthermometry was done by the application of a Linkam THMS600 heating-freezing device at LERA. For internal standardisation, synthetic, quartz-hosted H_2O , H_2O – NaCl and H_2O – CO_2 fluid inclusion reference materials (SynFlinC Standard collection) were taken for temperature correction of the measured data on a daily basis. The samples were cut perpendicular to the drill core orientation. Six representative, doubly polished thick sections (300–400 μm) were prepared and after petrography cut into wafers. The FIAs and the petrography of each fluid inclusion were determined by transmitted light microscopy following the approach of Goldstein and Reynolds (1994). The identified FIAs were classified as primary inclusions if exclusively hosted by propagating crystal growth zones (p), pseudo-secondary (ps), secondary (s), isolated inclusions (iso) or clusters (c) with no clear genetic relationship and no geometrical connection to growth zones or fractures (Walter et al., 2015). For each analysis, a triplet measurement was done to document the final melting temperature of ice ($T_{\text{m,ice}}$) and hydrohalite ($T_{\text{m,hh}}$), the CO_2 triple point (T_{tCO_2}), clathrate dissolution temperature ($T_{\text{m,Clath}}$) and the homogenisation temperature (T_{h}). Only fluid inclusion data that fulfil all quality criteria are processed. Repeated analyses are further done for the analyses showing a deviation of $<0.1^\circ\text{C}$ for $T_{\text{m,ice}}$, $T_{\text{m,hh}}$, T_{tCO_2} and

$T_{m,clath}$, and less than 1°C for T_h . It is important to note that a small amount of fluid inclusions show evidence for the metastable absence of hydrohalite due to the system-related phase diagram NaCl–H₂O–CaCl₂ (e.g. Steele-MacInnis et al., 2011) by application of Gibb's law. Hence, the metastable and therefore questionable data are excluded from any interpretation and further consideration and are also not presented in the raw data collection in the supplement. Pressure correction was applied by using the HOKIEFLINCS H₂O–NaCl program of Steele-MacInnis et al. (2012) with an estimated 1000 m sedimentary rock overburden in the Ibar Basin (Andrić et al., 2015).

Six samples were selected for bulk fluid crush leach analysis at LERA. Approximately 2 g of host mineral, calcite and colemanite, with a grain size of >1.0 mm, were hand separated and visible impurities were removed under the binocular. The optically impurity-free aliquots were cleaned for 3 h in milliQ water at 60–70°C. Subsequently, the samples were washed for 1 week in ultrapure water, changing the water at least twice a day to remove remaining cations on the grain surfaces. These pre-treated samples were dried and crushed to a fine powder in an agate mortar. Twenty millilitre of milliQ water was added to the powder in the agate mortar, from which 10 mL was used each for ion chromatography (IC) and for ICP-MS analysis at LERA. To suppress adsorption of doubly charged cations, crush leach solutions were acidified with 10 µL suprapure HNO₃ (Köhler et al., 2009; Ladenburger et al., 2020; Müller, Jacquemyn, et al., 2022; Müller, Walter, et al., 2022; Walter et al., 2023). The pre-treated and loaded solution was injected into a Methrom 930 Compact IC Flex chromatography system equipped with an 858 Professional Sample Processor and a Metrosep A Supp 5 column for quantification of anions (F, Cl, Br, J, NO₃, PO₄ and SO₄). For injection of the solutions into the Methrom 858 Professional Sample Processor, disposable syringe filters were used (CROMAFIL®Xtra RC-20/25 for anions; Ladenburger et al., 2020). Blank runs were carried out before and after each analysis, and defined standard solutions were regularly analysed to monitor the reproducibility and precision of the measurements. Uncertainties were usually smaller than 10% and effective detection limits were generally below 10 mg/L.

Trace element concentrations in the aliquot were measured with an iCAP RQ ICP-MS (Thermo Fisher Scientific) instrument equipped with a collision cell to eliminate polyatomic clusters. An ICP multi-element standard solution (Merck, Certipur) was used for calibration and regular quality checks. ¹⁰³Rh and ¹¹⁵In were used as internal standards for all measurement runs. The certified reference water CRM-TMDW-A

(High-Purity Standards, Inc.) was chosen to monitor the precision and accuracy of the individual measurements. Accuracy was between 1% and 3% in the measured sample suite. Absolute element concentrations in the original (non-diluted) fluid compositions are calculated using the microthermometry chlorine results as an internal standard.

4 | RESULTS

4.1 | Depositional environments in the study area

Based on the detailed sedimentological analysis of the three boreholes (IBM-2, IBM-6 and IBM-12, Figures 1 and 3–5) in the Piskanja deposit, Ibar Basin, 23 facies (Table 1) are distinguished, which are grouped into nine facies associations (FA, Table 2, Figure 6).

4.1.1 | Middle to distal alluvial fan environments

The medial to distal alluvial fan system includes amalgamated sheets, channels and floodplain deposits, that is facies association FA1 and FA2. These are observed in the lower part of the boreholes IBM-2 and IBM-6 (Figures 1 and 3–5). The sedimentary succession in the IBM-6 directly overlies the ophiolitic bedrock.

Amalgamated sheets and channels—multi-storey bodies

The facies association FA1 is dominated by amalgamated sheet-to-lense-like packages of red breccia, conglomerate and sandstone (F2, F3, F4, F5, F6, F7, F9, F10, Table 1, Figure 6A,B) intercalated with clast-supported conglomerate (F1, Table 1). Amalgamated sheets often include layer packages with angular fragments (Figure 6A). The clasts are fragments of hydrothermally altered andesite, fresh andesite, ophiolite, granite and metamorphic rocks to a lesser extent. The clast size ranges from 2 mm to ~30 cm. The lens-like packages show erosional to wavy lower boundary and a fining upwards grading trend. They may also include rip-ups of purple and light green mudstones of facies association FA2 and coal fragments. The preservation of finer-grained facies is low (F10, Table 1). In the vertical succession, FA1 alternates with FA2, FA3 and FA5.

The facies association FA1 is interpreted to be deposited from subaerial braided-stream flows and sheet flows, sometimes alternating with debris flow deposits in the medial to distal alluvial braid-plain environment (e.g. Blair & McPherson, 1994; Nemec & Postma, 1993;

TABLE 1 Facies distinguished in the studied sedimentary succession of Piskanja deposit in the Ibar Basin. The interpretation follows the studies of Bouma et al. (1962), Postma (1990), Miall (1996), Schieber et al. (2007), Renaut and Gierlowski-Kordesch (2010), Riding (2011) and Talling et al. (2012).

Facies code	Description	Depositional process
F1	Clast-supported pebble to granule-size conglomerate; subangular to subrounded clasts; medium sorting; structureless; randomly oriented clasts; polymict; often build discontinuous beds within medium-grained sandstone facies	Deposition from cohesionless debris flow
F2	Matrix-supported pebble (sometimes cobble) to granule size conglomerate; angular to subangular clasts, polymict; poor sorting; structureless; planar boundaries	Deposition from cohesive debris flow
F3	Medium-grained to fine-grained sandstone; moderate sorting; planar-cross bedding; sometimes erosional bases	Transverse bedforms
F4	Medium-grained to fine-grained sandstone; moderate sorting; through cross bedding; erosional bases; graded and ungraded	Channel fill
F5	Fine sandstones interbedded with siltstone and mudstone sometimes with scattered granules; laminated or massive	Deposition from a suspension of waning floods or abundant channel
F6	Medium-grained to fine-grained silty sandstone with floating pebbles, granules and mud rip-ups randomly distributed, structureless, plane bases	Subaerial to subaqueous cohesive debris flow
F7	Medium-grained to fine-grained sandstones; well-sorted, plane bases; structureless; rare rip-ups and granules	Subaerial to subaqueous cohesionless debris flow
F8	Amalgamated coarse to medium-grained sandstone; isolated pebbles and granules, rip-up clasts of mudstones; plane to erosive boundaries sometimes with loading casts; graded or ungraded	Deposition from high-density turbidity currents (Ta division of Bouma et al., 1962)
F9	Medium-grained to fine-grained sandstone; parallel lamination often delineated by organic-rich silt, coaly material, clay or carbonate mud; good sorting; planar base	Deposition from subaerial sheet or stream flow; sedimentation from high-density to low-density turbidity currents (Tb division of Bouma et al., 1962)
F10	Fine-grained sandstone to siltstone; ripple cross-lamination; good sorting	Deposition from low-density turbidity currents (Tc division of Bouma et al., 1962) or ripples—lower flow regime, overbank stream-flood deposits
F11	Siltstone to claystone with coaly laminae; parallel lamination; well-sorted; planar boundaries	Deposition from waning flows (stream, sheet, flashy); deposition by suspension fallout; sedimentation from low-density turbidity currents (Td division of Bouma et al., 1962)
F12	Dark grey to black claystone/marlstone; structureless or with planar lamination; plane boundaries; often organic-rich	Deposition from cohesionless debris flow; deposition from low-density turbidity currents (Te division of Bouma et al., 1962); suspension fallout; under redox conditions
F13	Medium-grained to fine-grained sandstone; flaser lamination often draped by clay, carbonate mud or organic material; good sorting; plane base	Reworking of sediments by wave action; deposition in fluctuating energy
F14	Medium-grained to fine-grained sandstone; lenticular lamination whereas sandstone lenses are engulfed in clay, carbonate mud or organic material; good sorting	Reworking of sediments by wave action, deposition in fluctuating energy
F15	Purple mudstone to siltstone; strings of granules and/or sand grains poorly sorted may be present; rare calcareous nodules; alternate with light green to beige siltstone to mudstone facies (F2)	Gradual settling of fine sediments in the floodplain deposit under oxic conditions; strings of coarser sediments resulted from the rapid fallout deposition from flash floods overflowing the floodplain
F16	Light green to beige siltstone to mudstone; laminated; alternate with purple mudstone facies (F1)	Gradual settling of fine sediments in the ponds along the lake margin

TABLE 1 (Continued)

Facies code	Description	Depositional process
F17	Light beige wavy to planar laminated mudstones, sometimes can be mottled with reddish flakes; no fossils; sharp and plane boundaries with units below and above; thickness up to 15 cm	Precipitation from the water column in a pond or shallow lake
F18	Grey to green structureless marlstone with dispersed organic matter	Deposition by suspension fallout
F19	Beige thinly bedded marlstone; sometimes includes burrowing features, desiccation cracks	Reworking of sediment due to bioturbation
F20	Light beige to beige laminated microbialite; wavy-crinkly lamination; sometimes discontinuous; the upper and lower boundary of laminae are diffuse	Deposition by microbial activity
F21	Thinly bedded to laminated porous carbonates (dolomicrites); sometimes with clotted texture; pores are sometimes filled with calcite, silica, boron mineralisation or bitumen; domal shape; moderate to sharp boundaries between laminae/beds	Deposition by microbial activity
F22	Intraclastic mudstone; carbonate mud clasts incorporated in siliciclastic mud to silt matrix; clasts are millimetre to centimetre in scale	Reworking and redeposition of carbonate mudstones
F23	Fragments of microbialite within mudstone matrix; matrix to clast supported, overturned or microfaulted laminae; clasts are millimetre to centimetre in scale	Reworking and redeposition of microbialite

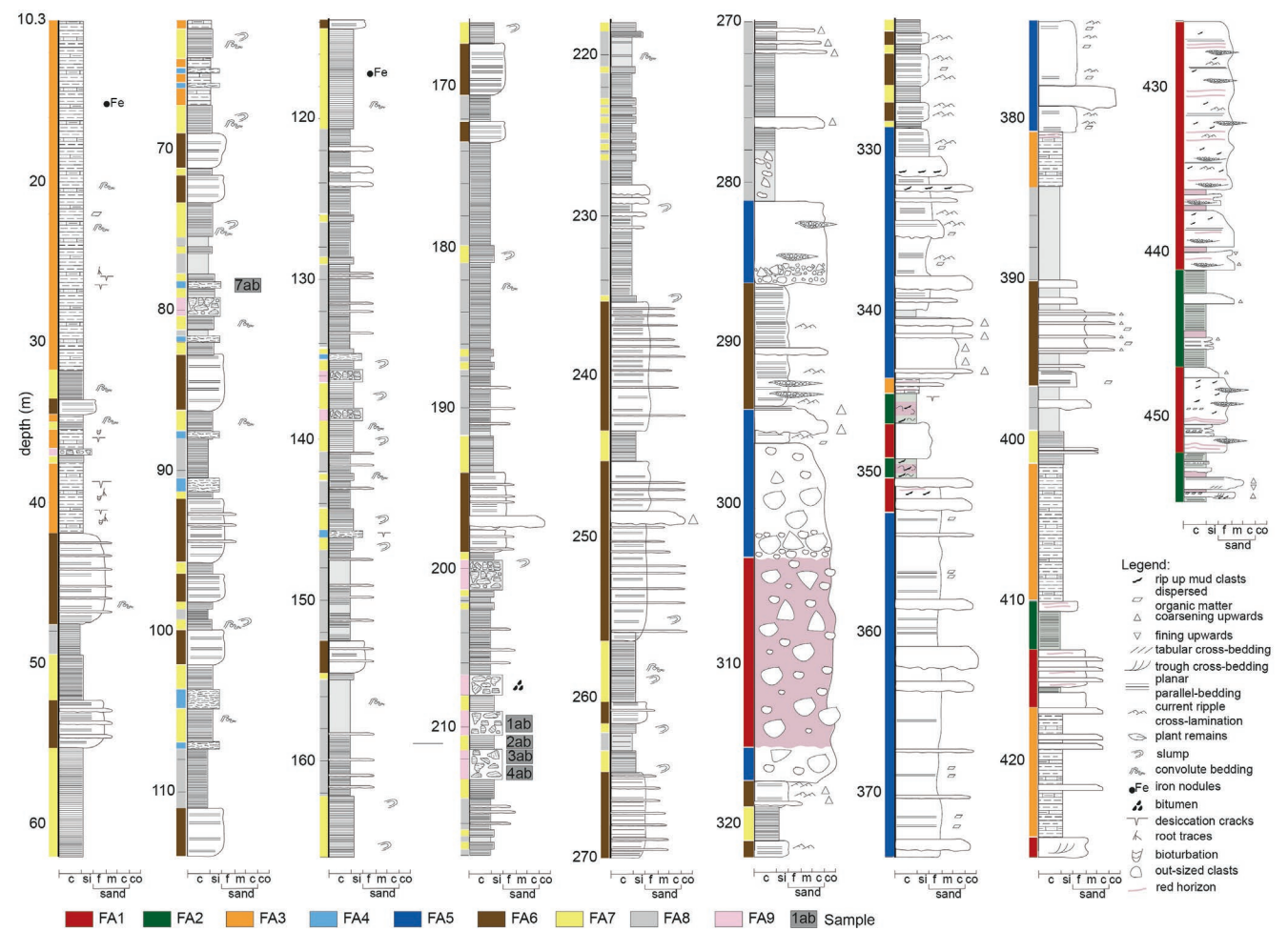


FIGURE 3 Sedimentary log, borehole IBM-2. See location in Figure 1. For the facies association abbreviation, see main text subchapter Depositional environments in the study area.

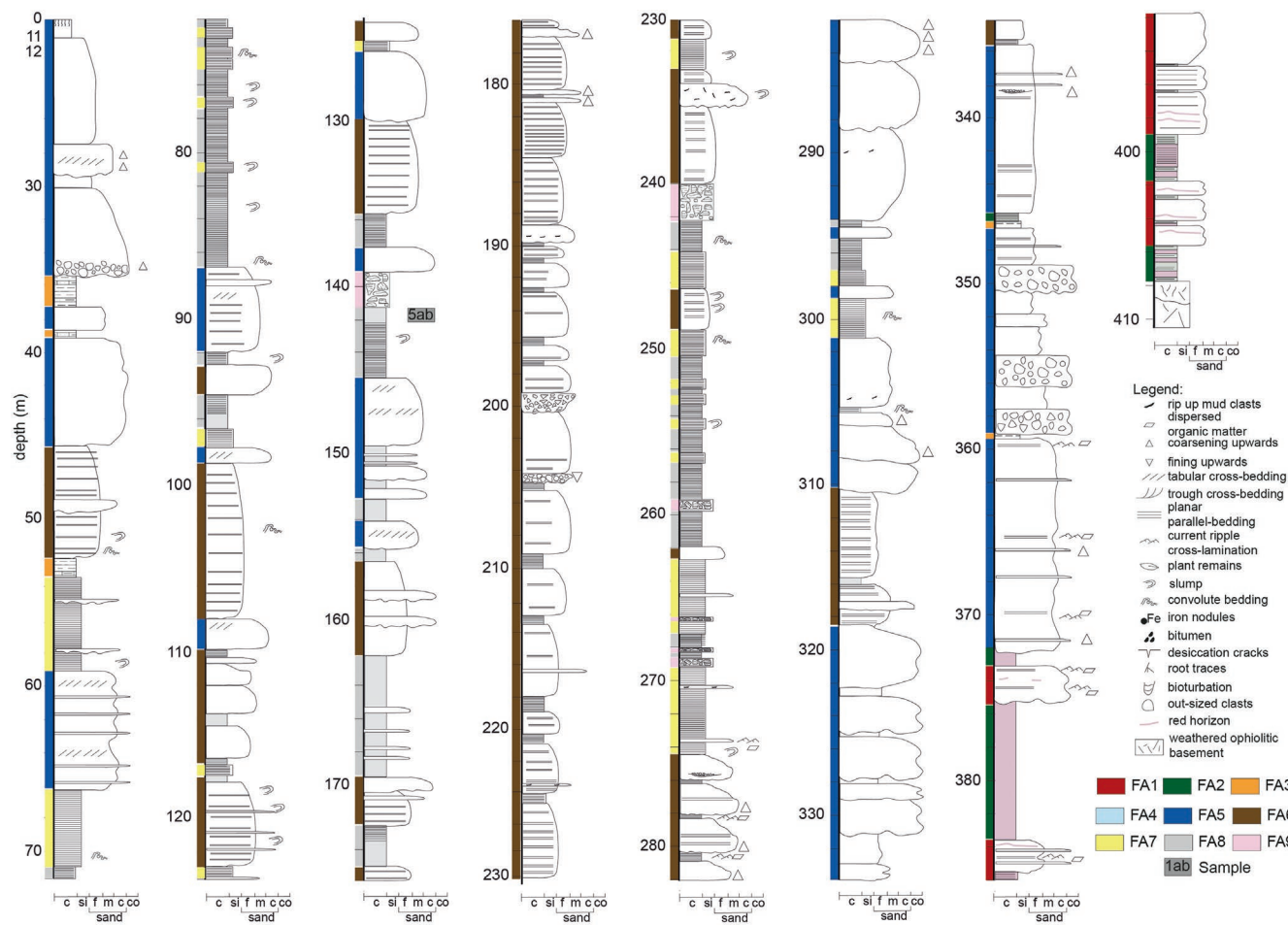


FIGURE 4 Sedimentary log, borehole IBM-6. See location in Figure 1. For the facies association abbreviation, see the section 'Depositional environments in the study area'.

Postma & Drinia, 1993). The sandstone and conglomerate are often mottled with intensive reddish colouring (Figures 3 and 6B), implying temporary subaerial exposure of the channels and soil development on the alluvial fan (e.g. Andrić, Matenco, et al., 2018; McCarthy et al., 1997).

Flood plain

The facies association FA2 is characterised by alternating light green to beige and purple siltstone to mudstone (F15, F16, F17, Table 1, Figure 6C) intercalated with thin sandstone layers (F5, F11, Table 1). Plant remains and coal fragments, when present, are aligned with bedding. This facies association alternates with FA1, FA3 and FA5 facies associations.

The facies association FA2 is interpreted to be deposited in the floodplains in the alluvial fan environment (e.g. Andrić, Sant, et al., 2017; Miall, 1996). The dominance of the fine grain-size facies with homogeneous to laminated plane bedding and lack of channels imply deposition from suspension fallout interrupted by sheet flooding events (e.g. DeCelles et al., 1991; Ielpi, 2012). The alternation of purple and homogeneous (with rare carbonate nodules)

and light green to beige-coloured and laminated siltstone to mudstone is interpreted to represent a shift from oxidising to reducing conditions. It suggests alternation of periods with subaerial exposure when pedogenic processes developed and calm deposition in ponds (e.g. Bentham et al., 1993; Ielpi, 2012).

4.1.2 | Littoral to sublittoral lacustrine environments

The littoral to sublittoral lacustrine depositional environments include marginal lake mudstones and sandstones (FA3), littoral to sublittoral microbialites (FA4), delta front (FA5), prodelta (FA6) and littoral to sublittoral oil shales (FA7), which are observed in all studied boreholes (Figures 1, 3–5 and 6).

Marginal lake mudstones and sandstones

Facies association FA3 is dominated by laminated and structureless grey to beige marlstone, siltstone and claystone intercalated with thin beds/laminae of

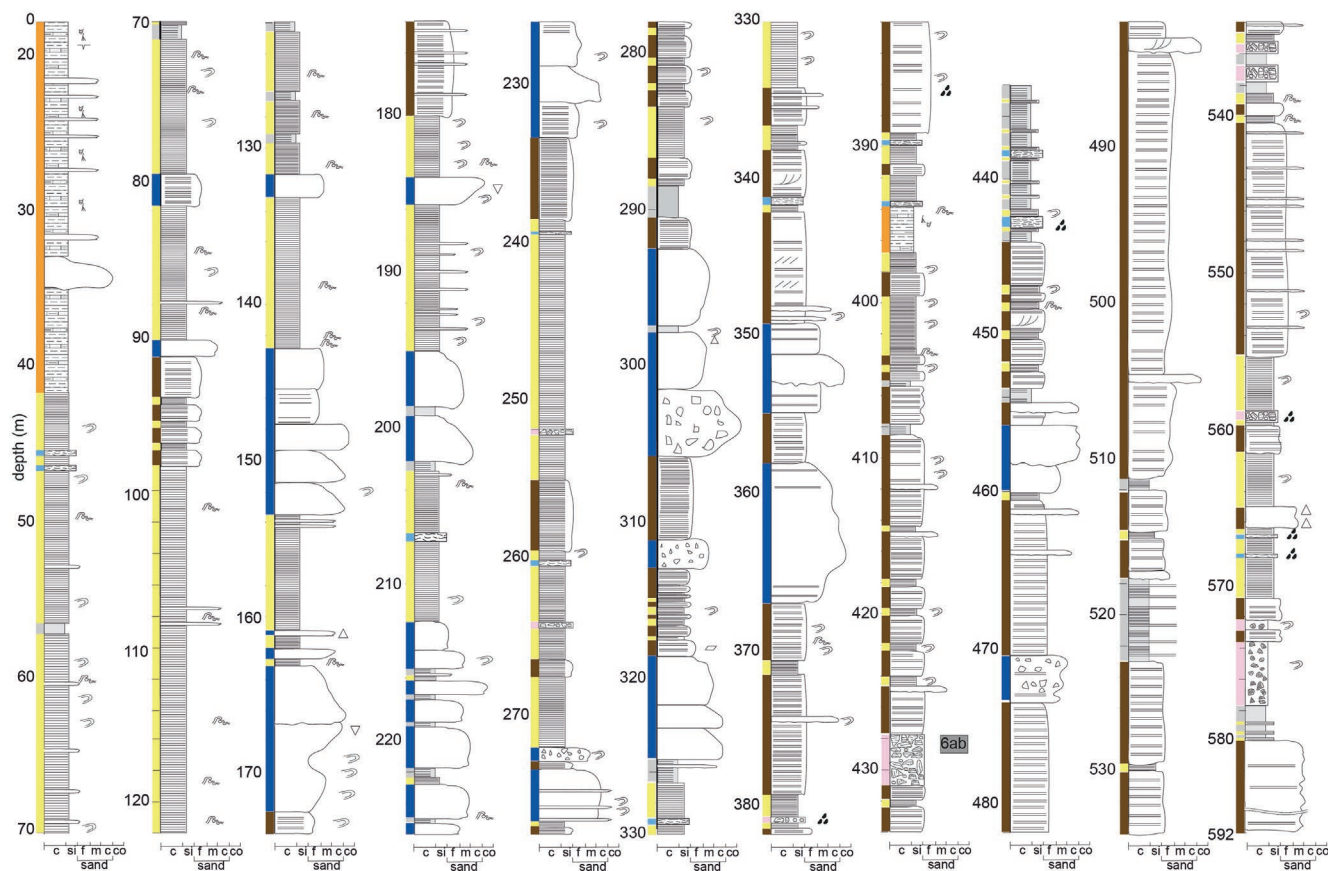


FIGURE 5 Sedimentary log, borehole IBM-12. See location in Figure 1. For the facies association abbreviation see the section 'Depositional environments in the study area'. For legend, see Figure 3.

fine-grained sandstone and rare bundles of laminated microbialite (F17, F18, F19, minor F9, F20, F22, Table 1, Figure 6D,E,F). Beds are wavy to tabular. Desiccation cracks, internal brecciation, roots and burrows often disrupt sedimentary structures (Figure 6D,F). Laminated microbialite is characterised by wavy-crinkly lamination that sometimes can be folded in broad open folds, up-turned and flipped-over structures. Rollover structures are less present (Figure 6F). Sometimes, this unit may be interrupted with a few centimetre thick convex-up carbonate structures of F21 of FA4. In the vertical succession, it alternates with facies association FA2, FA4, FA5, FA7 and FA9 (Table 2).

Facies association FA3 is interpreted to be deposited in shallow water lacustrine to the palustrine environment (e.g. Ielpi, 2012; Tānavsuu-Milkeviciene & Sarg, 2012). The presence of desiccation cracks suggests frequent subaerial exposure. The mottled mudstone with root traces with/without internal brecciation indicates the onset of the process of pedogenesis (e.g. Bohacs et al., 2000; Rhodes & Carroll, 2015). Intervals with the bioturbations imply an oxygenated shallow lacustrine environment (e.g. Smith et al., 2015). Wavy-crinkly carbonate laminae with a gradual transition to surrounding rocks indicate deposition

as a result of microbial activity. Furthermore, rolled over structures suggest destruction of the biolaminites by storm or flush flows (e.g. Schieber et al., 2007). This is supported by layers of fine-grained sandstone and siltstone that indicate distal fluvial influence by occasional flooding events (e.g. Melchor, 2007).

Littoral to sublittoral microbialite

Facies association FA4 is characterised by laminated or massive structures, where massive microbialite may show clotted fabric (F20, F21 sensu, Riding, 2011; Figure S1A,B,C). They are surrounded and intercalated with laminated or structureless marlstone, siltstone and claystone (F11, F18, Table 1, Figures 3–5, 6G,H). Microbialite has variable sizes on millimetre to decimetre scales. They display domal, laminated and anastomosing features (Figure 6G,H). Usually, they are highly porous, including fenestral porosity, intergranular porosity and/or vugs. Pore space is filled with dense organic matter, probably bitumen (Figure 6G) or mineralisation. Laterally, this facies association grades into FA3, FA7 and FA8.

Facies association FA4 is interpreted to be deposited in the lake littoral to sublittoral where microbial activity led

TABLE 2 Summary of fluid inclusion results.

Mineral	Assemblage	Fluid type	$T_{m,ice}$ (°C)	$T_{m,hh}$ (°C)	$T_{m,hal}$ (°C)	T_{co_2} (°C)	$T_{m,clath}$ (°C)	T_h (°C)	Salinity (NaCl + CaCl ₂)
Colemanite	Primary (p)	II	-0.2 to -1.3	-21.2 ^a	n.o.	n.o.	n.o.	6.4 to 82	0.4–2.2
Colemanite	Primary (p)	III-b	-6 to -21.2	-17 to -21.2	n.o.	n.o.	n.o.	153 to 261	9.2–23.8
Colemanite	Primary (p)	III-c	n.o.	-21.2	167 to 204	n.o.	n.o.	158 to 204	30.0–31.8
Colemanite	Pseudosecondary (ps)	II	-0.2 to -1.7	-21.2 ^a	n.o.	n.o.	n.o.	63 to 69	0.4–1.9
Calcite	Primary (p)	III-a	-1.2 to -13.3	-21.2 ^a	n.o.	n.o.	n.o.	143 to 183	8.2–17.2
Calcite	Primary (p)	III-b	-6 to -21.2	-8 to -12; -21.2 ^a	n.o.	n.o.	n.o.	140 to 213	9.0–24.7
Calcite	Primary (p)	III-c	n.o.	-21.2	169	n.o.	n.o.	169	30.4 (only 1 FI)
Calcite	Pseudosecondary (ps)	III	-7.5 to -12.3	-21.2 ^a	n.o.	n.o.	n.o.	191 to 217	11.1–16.2
Calcite	Cluster (c)	I	-0.1 to -1.1	-21.2 ^a	n.o.	-56.6 to 60.1	n.o.	65 to 86	0
Calcite	Cluster (c)	II	-0.3 to -1.7	-21.2 ^a	n.o.	n.o.	n.o.	69 to 86	0.5–2.7
Calcite	Cluster (c)	III	-3.7 to -18.7	-21.2	n.o.	n.o.	n.o.	168 to 263	6.0–21.5

^aHydrohalite is not observed (dissolved at the binary eutectic temperature) but set to -21.2°C due to the phase relations in the system NaCl-H₂O for quantifications.

to sediment binding, trapping and/or carbonate precipitation under low terrigenous influx (e.g. Cohen et al., 1997; Platt & Wright, 1991). The environment was oxygenated and nutrient rich, allowing the growth of microbes (e.g. Riding, 2011) in a shallow water environment (Renaut et al., 2013).

Delta front

Facies association FA5 is grey to greenish and comprises rounded to subrounded clasts to matrix-supported conglomerate and sandstone, often showing a coarsening-upwards trend and rarely intercalated with siltstone and claystone (F1, F2, F4, F6, F7, F8, F9 and minor F10, F11, F12, Table 1). The amalgamated beds can reach over 10m (Figures 3–5). These are often amalgamated sheets with rare channels filled by clast-supported subangular to subrounded conglomerate and sandy conglomerate (Figure 6L,J). Bed bases are planar to slightly erosional. Clast size in conglomerate ranges from granule to cobble (~30cm) with similar provenance as breccias and conglomerate of the FA1. The medium-grained to coarse-grained sandstone is often structureless and clast supported. These may include well-rounded outsized clasts and ripped-up mudstone/claystone clasts (Figures 3–5 and 6K). Dark matrix-supported breccia may appear. Clasts are angular and comprise hydrothermally altered andesite (Figure 6L). Medium-grained to fine-grained sandstone is also present, including normal grading, through cross bedding, and parallel bedding and/or lamination, while sandstone with ripple cross-lamination, climbing ripples, flaser and lenticular lamination is also common. The convolute bedding, water escape structures such as clastic dykes and sand injections are common. This facies association alternates with facies association FA1, FA3, FA6, FA7 and FA8.

Facies association FA5 is interpreted to have been deposited from the concentrated, high-energy flows during the phases of high river discharge in the delta front environment (e.g. Andrić, Sant, et al., 2017; García-García et al., 2006). Granular and turbiditic (high-density) flows were dominant depositional mechanisms in the delta front environment debris. Water escape structures imply rapid deposition and/or a high sedimentation rate (e.g. Pisarska-Jamroży & Weckwerth, 2013).

Prodelta

Facies association FA6 includes medium to fine sandstone alternating with siltstone, claystone and sometimes marlstone (F10, F11, F12, F13, F14, Table 1, Figure 6M). The thin (up to 10cm thick) intercalations of massive to normally graded medium to coarse sandstone and conglomerate (F8, F9, Table 1) may appear (Figures 3–5). Lenticular, flaser lamination, parallel and ripple cross-lamination are



FIGURE 6 Borehole samples (width is 6 cm) represent the facies and facies associations (see code descriptions in [Tables 1 and 2](#)).

(A) Red massive matrix-supported poorly sorted breccia conglomerate with angular fragments of hydrothermally altered andesite (green arrows), facies F2, part of amalgamated sheets and channels—multi-storey bodies deposited in middle to distal alluvial fan (FA1, borehole IBM-2). (B) Alternation of fine to coarse(pebbly) sandstone and red siltstones sporadically, including reddish soil rip-ups (red arrows) and mottled red horizons (dashed lines, borehole IBM-2) deposited in the FA1. (C) Green and purple mudstone to siltstone dominating flood plain environment (FA2, borehole IBM-6). (D) Alternating laminated marlstone (F19), intraclastic mudstone (F22) and microbialite (F20) overlaying likely deformed parallelly laminated fine sandstone to siltstone (F9) deposited in marginal lake FA8 depositional environment (FA3, borehole IBM-12). The disrupted layers by syndepositional deformation are delineated by red lines and arrows. (E) Wavy thin layers of microbialite (F20) with overturned layers (red arrows) overlain by silty marlstone (F19) deposited in marginal lake environments (FA3, borehole IBM-2). (F) Bioturbated mudstone, F19 deposited in marginal lake environment (borehole IBM-2). (G) Porous (F21) and laminated (F20) microbialite alternating with dark grey to brown marlstone (F18) deposited in littoral to sublittoral environment (FA4, borehole IBM-12). Pores filled with oil drops (red arrows). (H) Domal beige microbialite (F21) within deformed laminated siltstone to marly siltstone, deposited in littoral to sublittoral environment (FA4, borehole IBM-12). (I) Clast-supported polymict well-rounded conglomerate (F1) deposited in the delta front lake environment (borehole IBM-6). (J) Clast-supported polymict conglomerate (F1) passing into medium grained to fine grained through cross-bedded (F4) covered by clast-supported conglomerate (F1, marked by red lines) sandstone deposited in delta front environment of littoral to sublittoral environment (FA5, borehole IBM-6). (K) Medium-grained to fine-grained sandstone with flaser lamination (F13), covered by clast-supported conglomerate (F1) deposited in delta front environment. Rip-ups of sets of siltstone to fine sandstone and beige marlstone are delineated with red arrows (FA5, borehole IBM-2). (L) Dark matrix-supported breccia (F2), including fragments of hydrothermal altered andesite (white angular fragments) deposited in the delta front littoral to sublittoral environment (FA5, borehole IBM-6). (M) Lenticular bedding in prodelta depositional environment (FA6, borehole IBM-2) comprising coarse-grained to medium-grained sandstone lenses enfolded in laminated siltstone to mudstone (F14). (N) Alternation of dark claystone (F12), siltstone (F11) and medium-to fine-grained (F8) sandstone deposited in prodelta environment (FA6, borehole, IBM-2). (O) Oil shale, deposited in littoral to sublittoral lacustrine environment (FA7, borehole IBM-12). (P) Structureless silty claystone intercalated with fine-grained to medium-grained sandstone to siltstone deposited in a profundal lacustrine environment (FA8, borehole, IBM-2). Sandstones show erosional structures (red arrows), FA8. (Q) Clast-supported to matrix-supported breccia including fragments of oil shales and microbialites deposited in a profundal lacustrine environment (FA9, borehole IBM-12).

common. Siltstone and claystone are rich in dispersed organic FA7 and FA8.

Facies association FA6 is interpreted to be deposited in the prodelta depositional environment exposed to periodic high-density turbiditic flows (e.g. Andrić, Sant, et al., 2017; Mulder & Alexander, 2001). The high content of the dispersed organic matter suggests a greater influx of organic matter from the land (e.g. Rhodes & Carroll, 2015), probably due to erosion and redeposition of the older coal seams in the basin.

Littoral to sublittoral oil shales

Facies association FA7 is characterised by rhythmically laminated, beige to dark brown oil shale. FA7 includes couplets of organic-rich (darker) and clay-rich and carbonate-rich (mainly dolomite, Novković et al., 2024) mudstone (F11, F12, Table 1). Lamination is usually undulating and wavy, but in places, it may be plane and sharp. Kerogen-rich laminae are dominated by terrestrial organic matter (e.g. Andrić et al., 2015; Novković et al., 2024). In some situations, laminae comprise porous beige microbialite (F21), which laterally have variable thicknesses ranging between a few millimetres to centimetres (Figure 6O). The pores might be filled with oil drops. Sporadically, the laminae or thin beds including the particles of carbonate material flowing in the darker matrix occur (F22, F23, Table 1). Thin, millimetre-thick to centimetre-thick siltstone and fine sandstone layers and lenses are interbedded within FA7. These clastites are structureless or normally graded or show parallel lamination (F6, Table 1). Sometimes, sandstone and siltstone with cross-lamination, lenticular lamination or flaser lamination may be present (F13 and F14, Table 1). In the vertical succession, this facies association alternates with FA4, FA5, FA6 and FA8.

Facies association FA7 is interpreted to be deposited in a low-energy environment away from the area with high siliciclastic inflow and below wave base (e.g. Obradović et al., 1997; Tānavsuu-Milkeviciene & Sarg, 2012). The existence of thinner beds with redeposited carbonates implies their erosion and redeposition deeper into the basin, probably due to gravity flows. The rare thin intercalations of sandstone and siltstone support this interpretation. An association of mudstone with microbialite implies littoral to sublittoral zones (e.g. Muniz & Bosence, 2018; Riding, 2000). The preservation of organic matter in some laminae sets implies deposition in a low-oxygenated environment or anoxic conditions during their deposition (e.g. Graf et al., 2015). Terrestrial kerogen-rich mudstone is probably deposited by hypopycnal plumes basinwards of the location of fluvial input or during storm events by deposition of organic-rich mudstone from swampy areas around the basin (e.g. Renaut & Gierlowski-Kordesch, 2010).

4.1.3 | Profundal lacustrine environments

The profundal lacustrine environment includes dark siliciclastic turbidites (FA8) and gravitational mixed carbonates (FA9).

Profundal lake siliclastic turbidites

Facies association FA8 is dominated by dark grey to black laminated to massive claystone to siltstone (F9, F11, F12, Table 1). Dark to light grey silty laminae are parallel and sharp (Figure 6N). They alternate with black organic-rich claystone to siltstone laminae to thin beds. Sometimes a single or sets of wavy beige carbonate-rich laminae may appear in vertical succession. The FA8 is sometimes intercalated with fine-grained sandstone, well-sorted and up to 5 cm thick. Sandstone can be ungraded or normally graded but also may show parallel lamination, ripple cross-lamination and/or massive lamination (F8, F9, F10, Table 1). The base of the sandstone is sharp, in places erosional, or with load or flame structures (Figure 6P). Sandstone may include mudstone or oil shale rip-ups, coal fragments and/or microbialite fragments. This facies association, observed in all three boreholes, is vertically associated with FA6, FA7 and FA9.

Facies association FA8 is interpreted to be deposited from turbiditic flows associated with the background particle settling in the distal lacustrine environment. Structureless, normally graded sandstone to siltstone with rip-ups supports the interpretation of dominance of deposition from gravity flows (e.g. Mulder & Alexander, 2001; Talling et al., 2012) probably triggered by high river discharge (e.g. Andrić, Sant, et al., 2017). High organic matter content and preservation of lamination indicate profundal deposition at the anoxic water bottoms devoid of bioturbating benthic organisms (e.g. Graf et al., 2015).

Profundal lake gravitational mixed carbonate

Facies association FA9 (Table 2) occurs in shallower parts of IBM-2 and IBM-6, and deeper part of IBM-12 (~570–580 m, Figure 5). It comprises angular fragments of microbialite (FA4) and/or oil shale (FA7), sometimes contorted oil shale layer fragments (Figure 6Q and Figure S1D). Usually, the fragments are mud matrix supported (F23, Table 1). It can be porous in places where the pore space is often filled with oil and/or borates. In these situations, breccias may be monomict, including only fragments of oil shale or microbialite. Clast size varies from a few millimetres to a few centimetres. The thicknesses of the layers may reach up to 5 m. In the vertical succession, this facies association alternates with FA6, FA7, FA8 and FA9.

Facies association FA9 is interpreted to be deposited in the profundal zone due to the lack of any shallow water indicators (e.g. Gierlowski-Kordesch & Rust, 1994;

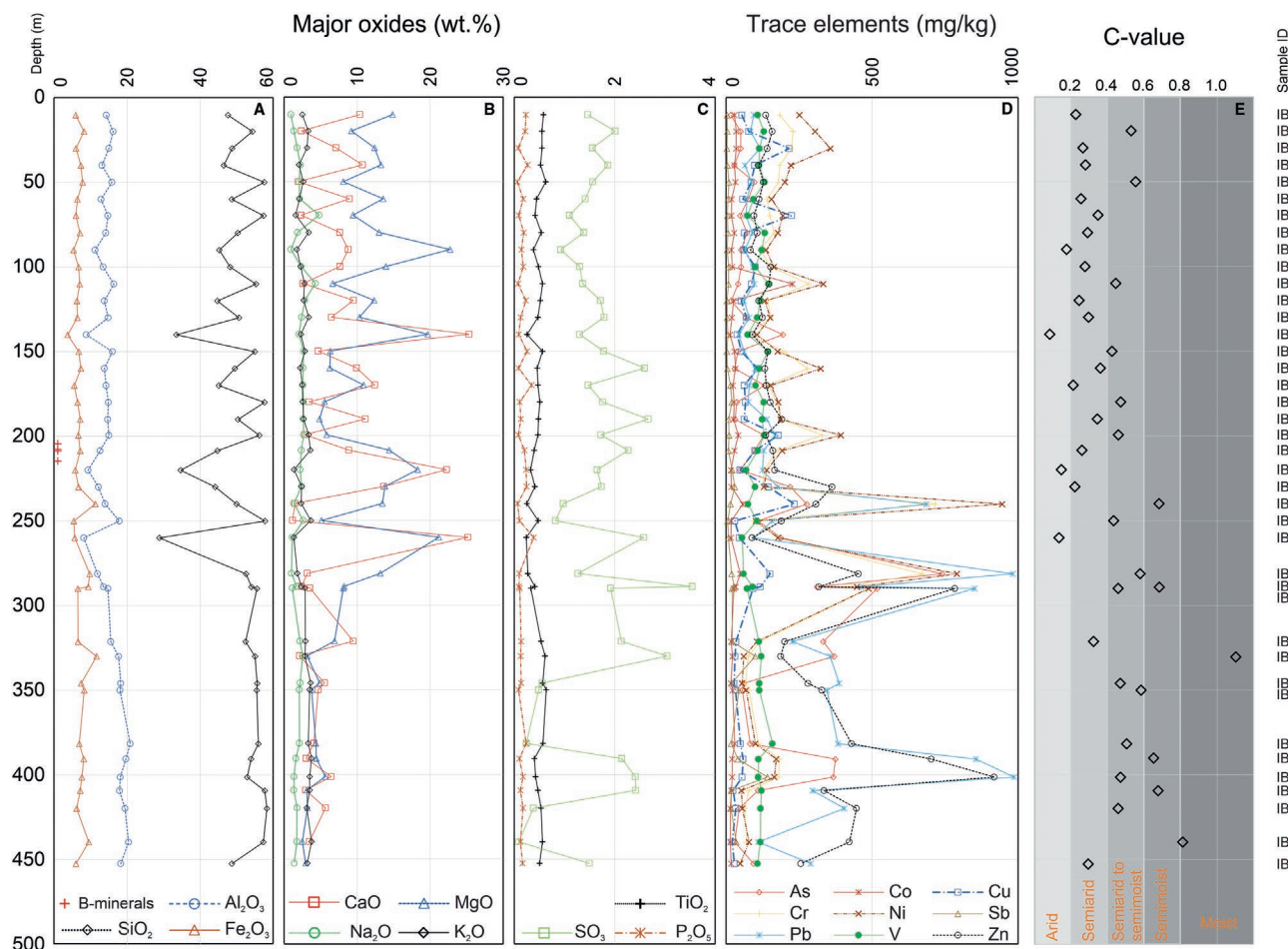


FIGURE 7 Variation of (A–C) major oxides, (D) selected trace elements and (E) C-value in the IBM-2 borehole; C-value = $(\text{Fe} + \text{Mn} + \text{Cr} + \text{V} + \text{Ni} + \text{Co}) / (\text{Ca} + \text{Mg} + \text{K} + \text{Na} + \text{Sr} + \text{Ba})$ (after Cao et al., 2012; Fu et al., 2016; Zhao et al., 2007).

Tānavsū-Milkeviciene & Sarg, 2012). Contorted oil shale beds are probably deposited by slumping and sliding processes likely along short distances triggered either by tectonically induced slope steepening, liquefaction of underlying mudstone, water column oscillations and/or over-pressure due to high sediment rates (e.g. Andrić, Matenco, et al., 2018; Bull et al., 2009; Gee et al., 1999). Angular fragments supported by mud matrix are suggested to be transported over longer distances by debris flow or high-density turbidity flow triggered by slumping (e.g. Talling et al., 2012; Tānavsū-Milkeviciene & Sarg, 2012).

4.2 | Major and trace elements in the borehole IBM-2

The major element oxides in sediments in borehole IBM-2 (Table S1; Figure 7) display SiO_2 (28.84–58.29 wt%), Al_2O_3 (8.15–20.88 wt%), variable MgO (2.49–22.74 wt%), CaO (1.16–25.33 wt%), Fe_2O_3 (3.75–11.68 wt%) and SO_3 (0.09%–3.55%). The high Ca and Mg content is found in carbonate-rich mudstones (mainly dolomite; Samples

IBM 2/14, IBM 2/22 and IBM 2/26; FA7 and FA8). The highest CaO content is determined in the sample from 140.0 to 140.5 m depth, while the highest MgO content is determined in the sample from 90.0 to 90.5 m depth.

The trace elements show variation through depth, especially As, Cu, Cr, Ni, Pb and Zn. Studied samples are highly enriched in As, Cu, Pb, Zn, Cr, Ni and Sb compared to Clarke values for black shales (Ketris & Yudovich, 2009). High contents of As, Cu, Pb and Zn are found in the samples from 281.3 to 290.5 m and 390.0 to 401.8 m depth. The highest Cu, Cr and Ni contents were found in samples from 240.0 to 240.5 m depth. The proxy for delineating humid and arid phases in the lake (Figure 7), $\text{C-value} = (\text{Fe} + \text{Mn} + \text{Cr} + \text{V} + \text{Ni} + \text{Co}) / (\text{Ca} + \text{Mg} + \text{K} + \text{Na} + \text{Sr} + \text{Ba})$, is calculated following the boundaries defined in Zhao et al. (2007).

4.3 | U–Pb geochronology

Three domains in sample IBAR 7ab, corresponding to needle sparite, black micrite and pore-filling calcite, were analysed for U–Pb geochronology (Figure 8, Table S3). The needle

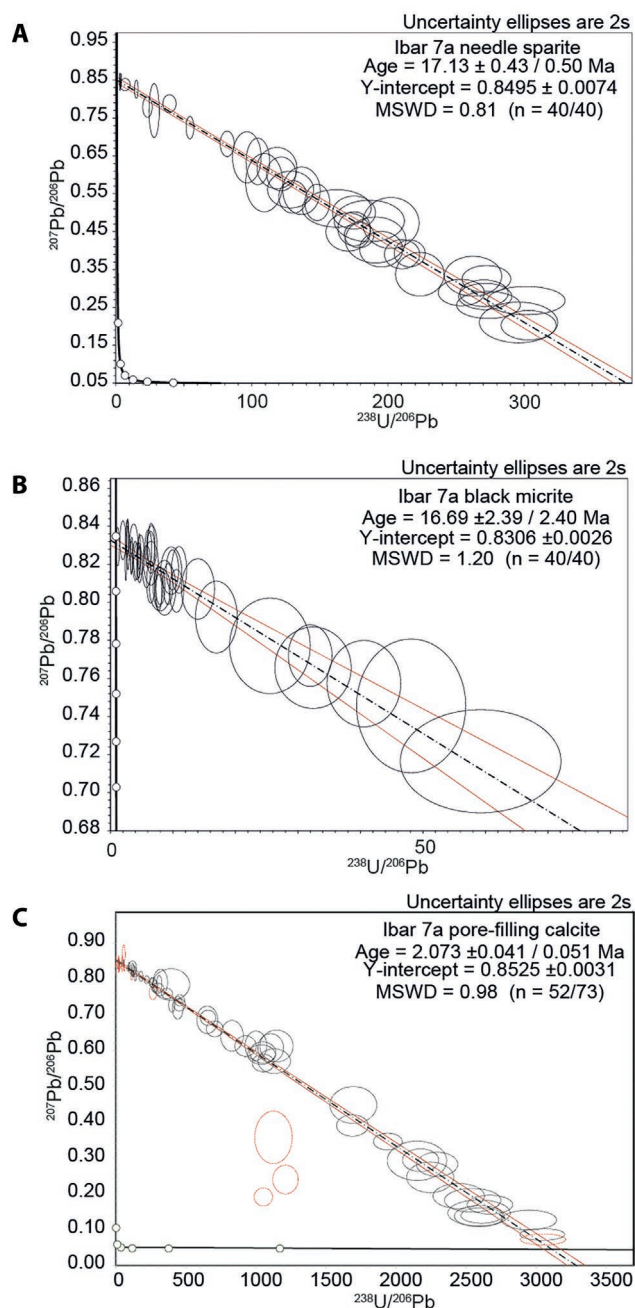


FIGURE 8 $^{238}\text{U}/^{206}\text{Pb}$ versus $^{207}\text{Pb}/^{206}\text{Pb}$ Tera-Wasserburg Concordia diagrams and corresponding absolute ages. The black dashed line represents the isochron. Red lines represent the envelopes of the regression lines (isochrons). Black ellipses represent the 'n' spot analyses and corresponding isotope ratios obtained. All ages are reported with 2σ confidence. Data point ellipses indicate 2σ internal uncertainty (95% confidence) of the isotope ratios on 'n' analysis. The black thick line is Concordia curve.

sparite and the black micrite give a similar age of within the uncertainty ca. 17 Ma. The U concentration found in the micrite is relatively homogeneous around $1.5\mu\text{g/g}$, while Pb is more variable ($0.18\text{--}3.4\mu\text{g/g}$). This resulted in a maximum spread in the $^{238}\text{U}/^{206}\text{Pb}$ ratio close to 60 and an age of 16.69 ± 2.40 Ma. In turn, the needle sparite shows a higher

concentration of U (mean of $3.7\mu\text{g/g}$) and lower Pb (down to $0.012\mu\text{g/g}$) contents, resulting in a higher spread on the X-axis of the Tera-Wasserburg plot (maximum of 303) and a more precise age of 17.13 ± 0.50 Ma.

On the other hand, the calcite filling the pores turned out to be distinctively younger, with the regression line cutting the Concordia at 2.073 ± 0.051 Ma. The U concentrations range from 0.007 to $0.66\mu\text{g/g}$, whereas the Pb concentrations are low, averaging $0.001\mu\text{g/g}$. Contrary to the micrite and sparite domains, where all the analysed spots were considered for age calculation, several spots were rejected for the pore-filling calcite. Although the petrographically cleanest areas were targeted, 21 spots show remarkably higher Th/U ratios, which probably reflect partial contamination by clay minerals.

4.4 | Macroscopic features of the studied samples

The samples are mainly located within dark claystone, siltstones and gravitational mixed carbonates (FA8 and FA9, Figure 9A,B,C,D,E,F,I). In one case, colemanite and calcite-rich veins cross-cut and/or are interbedded within the FA6 (Figure 9G,H). The observed minerals have a white matte colour and silky lustre. The studied samples show different textures, including massive zones of crystalline, tabular, columnar and needle-like colemanite; disseminated euhedral grains of colemanite; disseminated nodular colemanite and veins filled with colemanite. The colemanite fills faults and fractures that are observed in the deepest parts of the boreholes.

Massive colemanite consists of a white, unoriented structure with randomly arranged anhedral crystals of varying sizes and is densely packed. The texture is dominated by columnar colemanite (Figure 9A,D), while needle-like colemanite is less common and fills the space between columnar colemanite (Figure 9F). This texture is present within the FA9, gravitational mixed carbonates, including fragments of oil shales (FA7) and microbialite (FA4, Figures 3, 6Q and 4). The colemanite occurs as a late-stage precipitate in the interstitial space of calcite crystals within the pore space of microbialite or between fragments (monomict or polymict). The edges of the fragments are often obscured by colemanite.

The platy to tabular colemanite is zoned, with growth zones marked by a dark claystone matrix captured within the growth zones (Figures 3 and 9B,C). Crystal size reaches $2\text{--}3\text{ cm}$. The growth direction is perpendicular to bedding. Although carbonate fragments dominate the hosting facies association FA9 (gravitational mixed carbonates), colemanite appears to be intergrowing exclusively with the dark clay matrix.



FIGURE 9 Samples with boron minerals. (A) Ibar-1, IBM2_209_210.6 m, colemanite within brecciated oil shale/microbiolites, FA9. (B) Ibar-2, IBM2_210.6_211.3 m, tabular colemanite impregnated into oil shale and dark claystone. Green arrows show mineral growth zones and red arrows show mud matrix. (C) Ibar-3, IBM2_211.1_212.1 m, tabular colemanite within brecciated oil shale, FA9. Red arrows mark mineral growth, while green trapped mudstones. (D) Ibar-4, IBM2_212.6_213.0 m, colemanite within brecciated oil shale, FA9. Green arrows mark radially oriented columnar to needle-like colemanite. Orange arrows show tabular colemanite. (E) Ibar-5, IBM6_140.7–141.2 m, colemanite crystals within dark claystone. The red arrow shows fining upwards in colemanite crystal size. (F) Ibar-6, IBM12_428.2_429.1 m, colemanite in brecciated recrystallised and brecciated microbiolites and oil shale, FA9. (G) Prodelta facie association, FA6 cross-cut by the normal faults (IBM-12, 382.65 m, core width 6 cm, green arrows). A dashed red line represents the main fault zone, whereas thin light red lines show its Riedel shears. The main fault zone is filled by boron mineralisation (FP), which invaded the porous sand-rich layer in the footwall (LP) leading to layer parallel accumulation of boron mineralisation. Light blue arrows show possible fluid flow. (H) Colemanite planar (green arrow) and anastomosing (pink arrow) veins cross-cutting prodelta facies association, FA6 (IBM-12, 346, 70 m depth, core width 6 cm). (I) Disseminated colemanite nodules (green and pink arrows) within dark claystone, FA8 (IBM-12, 453.10 m, depth, core width 6 cm).

Disseminated colemanite crystals are rhombohedral, floating in dark claystone and siltstone of facies association, FA8 (Figures 4, 6P and 9E). The crystals are euhedral to subhedral, and their size varies from millimetre to centimetre. The crystals show no preferred orientation. Crystals are not always isolated; in the case of larger crystals, they seem to coalesce, forming layers. However, the crystal size decreases upwards in stratigraphy, showing ‘normal grading’ (Figure 9E), while the amount of dark claystone matrix increases.

Colemanite is also associated with active normal faults, where it cements the porous fault zone and neighbouring porous lithologies, mainly in the footwall

(Figure 9G). Colemanite displays flaky to rosette morphology. The mineralisation has diffuse boundaries towards the host rock.

Fibrous colemanite fills fissures cross-cutting the sandstones, pebbly sandstones and siltstones of the prodelta facies association, FA6 (Figures 6M and 9H). The thin veins (1–2 mm) are planar and anastomosing and cross-cut the sedimentary structures of the host rock (green and pink arrows, Figure 9H).

Nodular colemanite is disseminated within the dark claystone and siltstone facies association, FA8 (Figures 6P and 9I). The colemanite has an irregular cauliflower appearance, with sizes ranging from a few millimetres to

1 cm. Nodules are isolated within the host rock. Larger nodules deform the host rock (pink arrow in Figure 9I). Zones with smaller and larger nodules are separated.

4.5 | Petrography

Figure 10 shows that the SEM analysis of the Ibar –1–6 samples distinguishes colemanite and calcite as the dominant minerals.

Early calcite I is coarse grained, anhedral and contains inclusions of Fe-hydroxides. The growth of the crystals is unidirectional. Tiny boron phases (not possible to identify) fill the vugs. Large euhedral crystals of colemanite I (several centimetres in size) grow on the top of calcite. The crystals are of high purity and do not show any other

phases included. No growth zones are visible in SEM. Rare strontianite and celestine are recognised on fractures in colemanite I and in the interstitial pore space. On top of the colemanite, I unzoned feldspar (up to 4 mm) is recognised, which is overgrown by clay minerals assemblage (phases not identified), tiny colemanite II (<150 µm), ulexite (<20 µm) and borax (<10 µm). Euhedral pyrite occurs as rare crystals with sizes <5 µm. Calcite II overgrows the last-named minerals in the interstitial vugs, and quartz occurs in fractures cutting the whole sequence.

4.6 | Fluid inclusion petrography

Primary fluid inclusions are hosted in calcite I (pCal1-1) and colemanite I (pCol1-1, Figure 11). Pseudosecondary

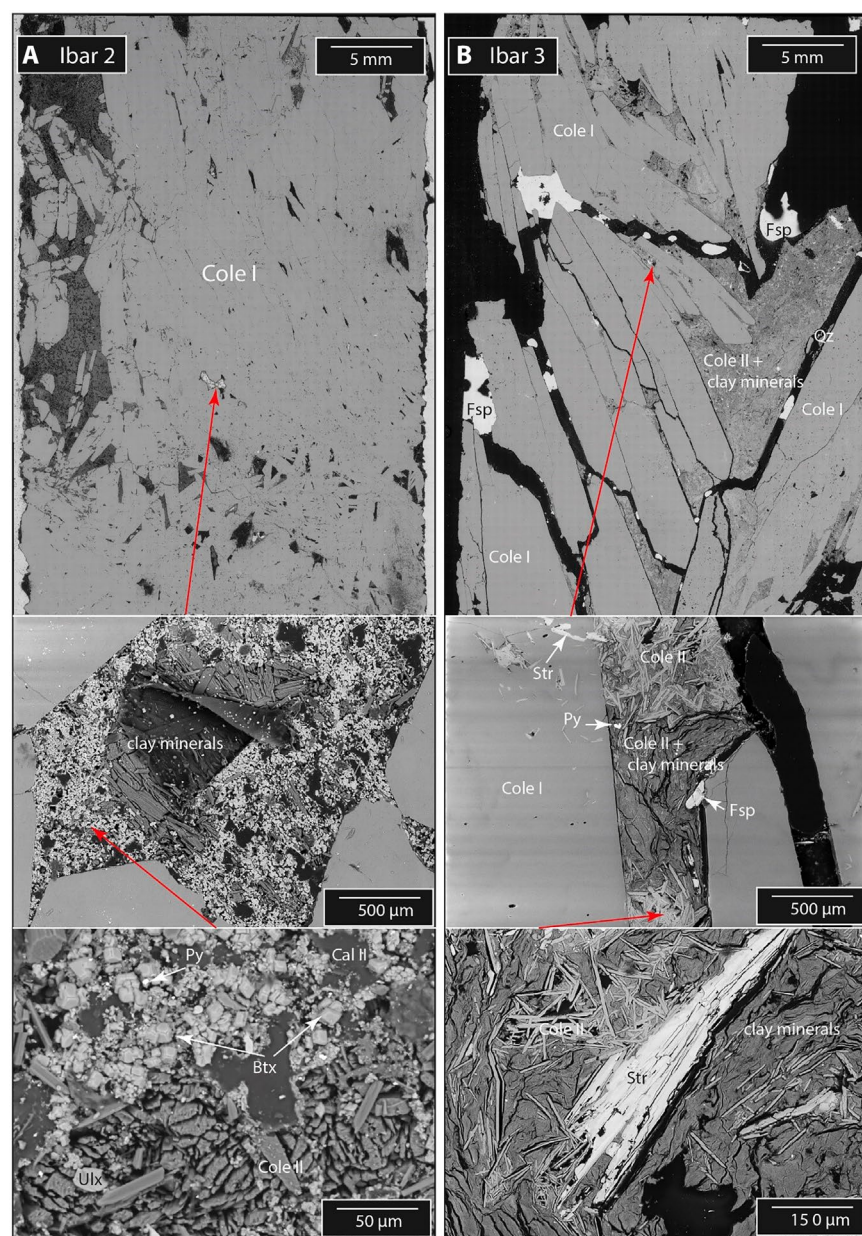


FIGURE 10 SEM images of sample Ibar 2 (A) and Ibar 3 (B). In both samples, colemanite has a columnar texture (tooth shaped), including elongated crystals. In the interstitial space, filled with colemanite II, clay minerals and strontianite, locally fine-grained borax and ulexite occur as late-stage filling. Cole, colemanite; Ulx, Ulexite; Btx, borax; Py, pyrite; Fsp, feldspar; Str, strontianite; Qz, quartz.

FIA in calcite (psCal1-1) reflect crack-seal processes prior to colemanite I formation but post-date primary fluid inclusions in calcite. Pseudosecondary fluid inclusions in colemanite I also occur frequently (psCol1-1). As is common for calcite, numerous fluid inclusions are organised in clusters (cCal1-1), depicting a former crystal shape. Secondary FIAs in calcite I and colemanite I are monophase and therefore not analysed.

4.7 | Microthermometry

Fluid inclusion sizes vary between 5 µm and 80 µm, independent of the petrographic position and inclusion shape (no systematics). Fluid inclusions for which post-entrapment modifications cannot strictly be ruled out were excluded from further analyses and interpretation. The fluid inclusions are subdivided into three types (I, II, III) based on their composition (Figure 11). Type III inclusions have three subtypes (III-a, III-b, III-c). Type-I fluid inclusions are CO₂ bearing and vapour rich, Type-II

fluid inclusions are mono-phase aqueous inclusions and Type III fluid inclusions show a H₂O-NaCl composition. Based on variable phase transitions observed at room temperature, Type-III was subdivided into subtypes. Type III-a has a low homogenisation temperature (148–183°C, Figure 12) and a salinity of 8.2–17.2 wt% NaCl + CaCl₂ and a small bubble (L₉₅V₀₅). Type III-b contains a two-phase assemblage with a high homogenisation temperature (153–261°C) and a salinity of 9.0–24.7 wt% NaCl + CaCl₂. Type III-c has a two-phase assemblage (including halite daughter minerals) at a homogenisation temperature of 158–204°C and high salinity (30.0–31.8 wt% NaCl+CaCl₂) with a high liquid–vapour ratio (L₉₀₋₉₅V₀₅₋₁₀).

4.8 | Crush-leach analysis

As fluid inclusion types I and II are of very low salinity, the measured fluid compositions represent the chemical bulk ratios of the medium to high salinity fluid inclusions (Type III-a, III-b, III-c, Figure 12). The Cl/Br mass ratios

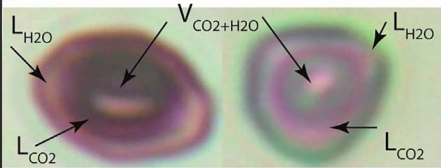
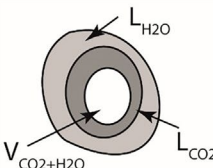
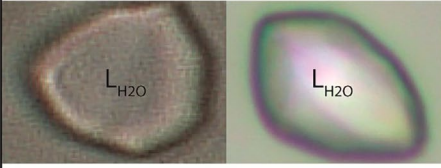
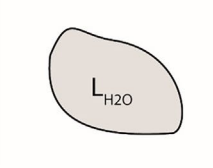
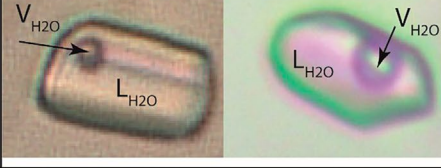
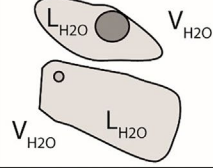
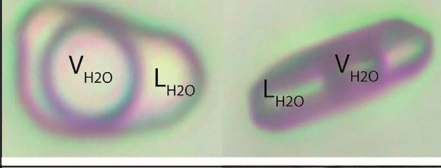
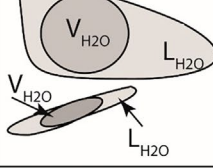
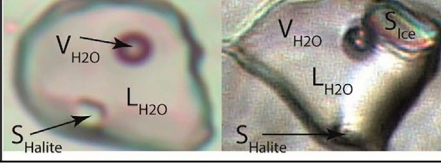
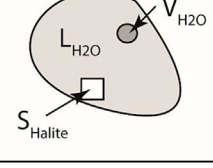
Types	Representative Fluid Inclusions (Size varies from 5 to 50 micron)	Schematic Inclusions
Type I, CO ₂ -H ₂ O		
Type II, H ₂ O (monophase)		
Type III-a, H ₂ O-NaCl low Th, low volume fraction		
Type III-b, H ₂ O-NaCl high Th, large volume fraction		
Type III-c, H ₂ O-NaCl high salinity		

FIGURE 11 Fluid systematics in the studied samples.

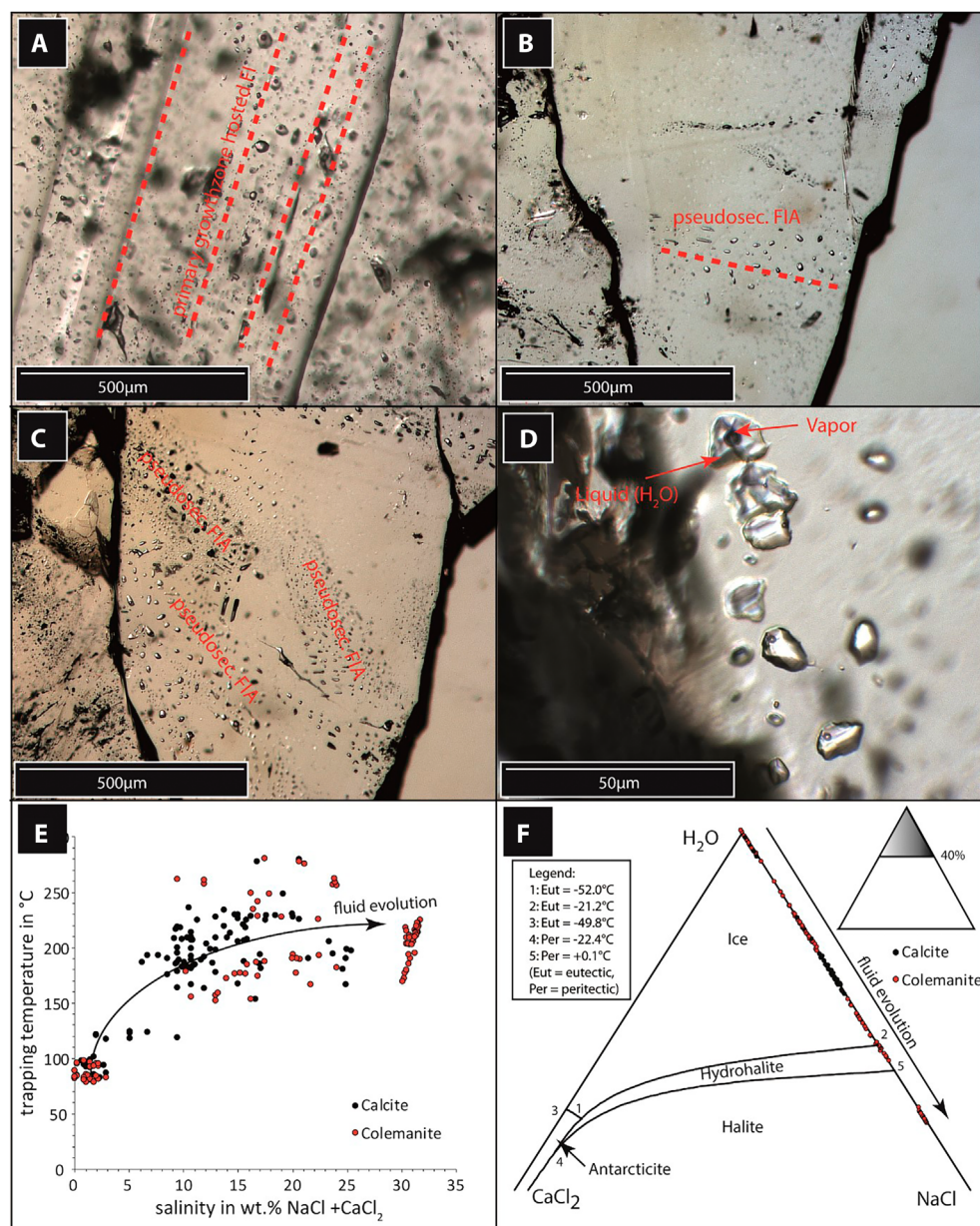


FIGURE 12 (A–D) Fluid inclusion petrography. (E) Trapping temperatures versus salinity. Note evolution towards higher salinities during crystal growth. (F) The fluid composition reaches halite supersaturation during the system's evolution.

scatter between 312 and 51. Cl/J mass ratios show a spread between 39 and 117, whereas Rb/Cs mass ratios also show a remarkable scatter between 7 and 18. The Na/Mg ratio is also low, with 2–8.8, with one outlier at 215.

5 | DISCUSSION

In this section, firstly, we discuss depositional environments observed in the boreholes from the Piskanja deposit, Ibar Basin. This is followed by discussing the new absolute ages and processes governing boron precipitation in the Piskanja deposit. Finally, we present the synthesis

of the geological evolution of the Piskanja Ibar Basin with the implication of the late-stage evolution of an orogen, that is the Dinaridic orogen.

5.1 | Depositional environments

The studied boreholes from the Piskanja deposit in the Ibar Basin reveal a conformable evolution from an alluvial environment to a delta fan and dominantly lacustrine environment (Figures 3–5 and 13). Only borehole IBM-6 provides information about the directly underlying bedrock, which is, in this case, weathered ophiolite (Figure 4).

This is expected given the borehole's position being closer to the basin margin compared to the other two boreholes (Figure 1C). The two main lake stages (open and closed stratified lake) are identified based on variations in facies association distribution, siliciclastic input, degree of lake restriction and salinity. Stages are defined by sedimentological characteristics and depositional trends controlled by the interplay between climate and tectonics.

Stage 1, that is the open lake stage, is pre-dated by the alluvial fan system observed in the southern and eastern parts of the subbasin, in IBM-2 and IBM-6. The alternation of coarse-grained, middle alluvial fan and fine-grained, floodplain facies associations implies either rapid change in environmental energy (e.g., Longhitano et al., 2015) or lateral migration of the alluvial fan (e.g., Miall, 1996). The changes in environmental energy may be induced by variable precipitation rates, which are typical for arid to semi-arid environments (e.g., Schlunegger et al., 2017) and/or tectonic activity increasing the depositional slope and rejuvenating the source area (e.g., Andrić, Sant, et al., 2017; Andrić, Matenco, et al., 2018). Arid to semi-arid climatic conditions characterised by alternating relatively humid and dry phases may be inferred from the interfingering of purple to reddish (with pedogenic features, F15, Table 1) and greenish mudstone to claystone (F16, Table 1, e.g. Ventura et al., 2018). The sediment transport was likely short and the sediment source is restricted to the surrounding bedrock units based on angularity and nature of

the fragments. This is also visible in the distribution of the major and trace element analysis in the IBM-2. The peaks in SiO_2 , Al_2O_3 , Pb, Zn, Cu, Ni and Cr (Figure 7) correlate with the high clastic input derived from granodioritic, andesitic and ophiolitic bedrock. To the east, as observed in the IBM-2, the alluvial conditions are several times interrupted by rising lake levels marking the onset of a lacustrine phase. This is recorded by the alternation of alluvial sedimentary packages and lacustrine environments (four lake level rises, metre scale in thickness, Figures 3 and 13), generally having an overall aggradational to progradational depositional trend. The packages show pedogenic features implying frequent subareal exposure. In the lowest part of IBM-2, the first two lake rising cycles are marked by the alternation of alluvial and littoral to sublittoral lacustrine environments (marginal lake mudstones and sandstones and littoral to sublittoral oil shales) away from the clastic influx. In the profundal, siliciclastic turbidites were deposited and are dominated by mudstone-rich facies intercalated with isolated normally graded erosion-based sandstones and carbonate-rich wavy laminae. This is followed by relative lake level fall and subsequent rise cycles marked by the alternation of alluvial and deltaic environments, implying increased sediment supply rates over accommodation change rates. In IBM-6, the direct transition from an alluvial to a delta fan system (Figure 4) suggests that the sediment supply from the south remains high during lake level rise intervals. The increase in roundness of the

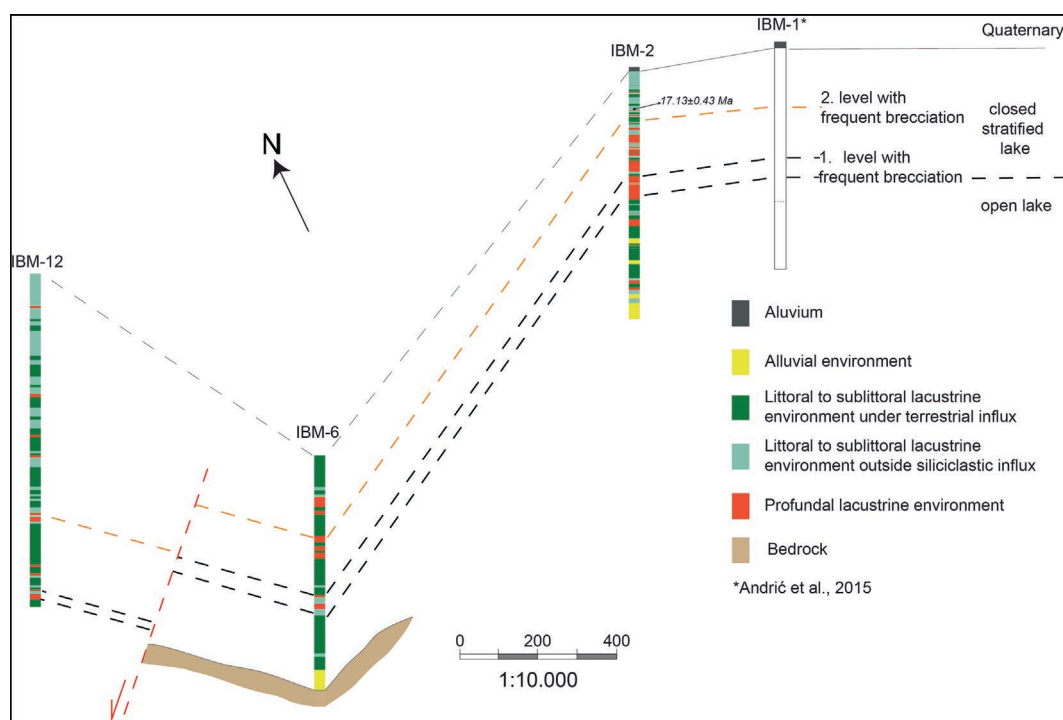


FIGURE 13 A correlation panel between the studied boreholes, through the study area.

delta components compared to their alluvial counterparts implies longer transport and reworking along the lake shores. The sediment supplying delta fans was induced by periods of high precipitation rates (e.g. Renaut et al., 2021). The tectonic contribution expressed by the activity of the basin boundary fault systems cannot be excluded (e.g. Andrić, Matenco, et al., 2018; Andrić, Sant, et al., 2017).

The beginning of Stage 2, that is, a closed stratified lake, is marked by an increase in the frequency of gravitational mixed carbonates within the lake's profundal environment following the lake's expansion during the previous stage (Figure 13). This is marked by the alternation of deltaic depositional environments (delta front and prodelta), gravitational mixed carbonates, littoral to sublittoral lacustrine (microbialites and oil shales) and profundal environments (siliciclastic turbidites and gravitational mixed carbonates) in all three studied boreholes. The packages dominated by deltaic deposits imply high sediment supply and water discharge, probably reflecting the periods of high precipitation rates and/or tectonic activity (e.g. Andrić, Sant, et al., 2017). The delta system distally grades into profundal organic-rich claystones intercalated with turbiditic flows (profundal lake siliciclastic turbidites, FA8, Table 2). The predominantly terrestrial organic matter (Andrić et al., 2015; Novaković et al., 2024) was transported as a suspension into the lake profundal by hypopycnal delta plumes (Figure 15A). The organic matter preservation implies anoxic bottom conditions and deposition under the pycnocline, implying lake stratification (e.g. Graf et al., 2015). The scarcity of fossil remains (e.g. Gagić, 1985) also suggests stratified profundal lake conditions, which are also observed in other lakes (modern lake Zurich, Kelts & Hsü, 1978; Tanganyika, Huc et al., 1990; Tipton Member, Great Green River Basin, Graf et al., 2015).

Laterally, in the littoral areas, protected from the clastic sediment supply from the land, microbes thrive in oxygenated and nutrient-rich environments building microbialites (e.g. Platt & Wright, 1991; Riding, 2011). These stromatolitic facies were deposited in a shallow environment during rather short humid seasons when fresh water was delivered into the lake by deltas, as also observed in the lakes of the East African Rift (Renaut & Owen, 2023). Distally, the sublittoral environment is dominated by oil shales, indicating mixed carbonate and siliciclastic deposition. Their carbonate-rich laminae were dominated by dolomite/dolomiticrite (Novković et al., 2024). The dolomite is probably developed through biogenic activity in the high alkaline and/or saline environment also seen in modern lakes (Diloreto et al., 2021; Guo et al., 2023; Roberts et al., 2013). Several studies emphasise the importance of hydrothermal activity in the formation of primary dolomites

(e.g. Guo et al., 2023; Yang et al., 2021). The lack of evaporitic mineral casts and large-scale desiccation features within basinward associations excludes the playa model to explain dolomite generation. Basinward oil shales intercalate with profundal zone organic-rich mudstones and gravity flows, that is turbidites and slumps. The profundal area is affected by frequent periods of depositional slope instability, which are marked by sliding and slumping varying greatly in their thickness. Many probably witness events related to the liquefaction of underlying mud-rich deposits, overpressure due to the high sedimentation rate (e.g. Bull et al., 2009; Gee et al., 1999). Furthermore, two brecciation levels are observed in the studied boreholes (Figure 13). It is distinct by the presence of gravitational mixed carbonate facies association (FA9 sometimes >5 m thick, Figures 3–5, 6Q and 13), occurrence of borates, followed by progradational to aggradational deltaic deposits. These levels alternate with littoral to sublittoral oil shales and organic-rich profundal lake siliciclastics dominated by mudstones, often including borates as well. This depositional sequence implies a lack of sediment supply alternating with periods of erosion of the littoral to sublittoral microbialites and oil shales probably following their exposure to wave action. Such basin-wide event is probably induced by lake level drop and/or slope steepening due to the activity of the marginal faults (Andrić, Matenco, et al., 2018).

The two slump levels divide the closed stratified lake stage into two complex cycles observed in all three boreholes. The dominance of the profundal facies associations and littoral to sublittoral microbialites and oil shales in the IBM-2 borehole implies that this borehole became more protected from the siliciclastic input during the basin evolution. This is also visible in the distribution of the major and trace element analysis, where CaO and MgO peaks become prominent (Figure 7). In contrast, elements implying clastic input (SiO_2 , Al_2O_3 , Pb, Zn, Cu, Ni, Cr) derived from erosion of bedrock show significantly lower values (Figure 7). The occurrence and thickness of the profundal facies associations vary and alternate mainly with oil shales, microbialites and delta indicating fluctuating and unstable lake level conditions.

5.2 | Processes responsible for borate precipitation

The textural features of the borate imply their syn-depositional and post-depositional character. Syndepositional borates are associated with profundal lacustrine facies associations deposited under anoxic conditions. The syndepositional borate textures include

disseminated colemanite crystals, nodular colemanite and platy to tabular, while massive colemanite texture may imply its syn-depositional and post-depositional origin. Post-depositional borates are associated with the faults cross-cutting various facies associations. They include fibrous and flaky to rosette structures and are associated with faults and fissures in the stratigraphic succession's lower part.

The disseminated colemanite within the claystone matrix (Figure 9E) is formed by non-competitive growth and precipitation on the lake bottom under conditions of progressive oversaturation (e.g. Helvacı & Ortí, 2004). Colemanite cumulates deposited on the mud-rich bottom of a stratified perennial (hyper)saline lake are also typical for other evaporitic minerals. Variation in the crystal sizes likely resembles variation in precipitation rates (e.g. Helvacı & Ortí, 2004). A similar disseminated texture is also observed in the Loma Blanca deposit in the La Punta region (Alonso et al., 1988).

The nodular colemanite (Figure 9I, pink arrows) formed in unconsolidated sediments beneath the water–sediment interface is a result of dense, concentrated brines saturating the sediment pores. The examples from the Bigadiç deposit in western Anatolia (Helvacı & Alonso, 2000) and Furnace Creek, Death Valley, CA (Tanner, 2002) demonstrated that the growth probably continues during compaction. The variations in nodule size imply variations in chemical conditions probably associated with the variations in the chemistry and influx of the basinal fluids.

Platy to tabular colemanite shows evidence of bottom growth at the muddy lake bottom or filling pore space of profundal lake gravitational mixed carbonates. The fluid inclusion data indicate a rise in fluid temperature up to 180°C, implying that a significant portion of the mineral formed during diagenesis. An association with the oil drops supports this. During its growth, it trapped strontianite, feldspars and clay minerals (Figure 10). The presence of secondary ulexite and borax growing on top of the large colemanite crystals (colemanite I, Section 4.5) implies that, in time, Na concentrations in brine increased.

Massive colemanite grew either beneath the depositional surface in the unconsolidated sediment or filling the pore space of profundal lake gravitational mixed carbonates.

5.3 | Evolution of the bittern brine

The fluid inclusion study on the massive and tabular colemanite reveals that early trapped primary fluid inclusions in colemanite and associated calcite indicate an initial precipitation beginning at *ca* 3 wt% salinity and temperatures of about 80–100°C (Figure 12E). The geochemistry

of the brine shows a continuous evolution from low to high salinities (up to 31 wt% NaCl+CaCl₂) with decreasing Cl/Br ratios from about sea water composition (288) down to 51, which probably reflects a successively evaporated bittern brine (Bons et al., 2014; Walter et al., 2016, 2017 and references therein). This evolving bittern brine is regularly trapped during crystal growth and propagating diagenesis until 200–220°C is reached, where the system is shut down (Figure 12E). Previous vitrinite reflectance and fission track data suggested that during basin burial, the maximum average temperatures in the Piskanja sedimentary succession were around ~100–110°C (Andrić et al., 2015). Local temperature maximums are detected along the basin margin near the IBM-2, reaching temperatures above 120° at ~7 Ma. Andrić et al. (2015) linked this local maximum with the hydrothermal fluids probably localised along the basin bounding fault zone. Furthermore, the oil pockets in the basin (e.g. Novković et al., 2024) imply that local temperature reached oil window conditions, which agrees with the temperature ranges derived from our fluid inclusions.

The interpretation of an evolving bittern brine is further supported by a high Cl/I ratio (39–117), which reflects the fluid's low iodine content and, therefore, no influence of halides (because iodine is often elevated in evaporate units). Based on the geochemical fingerprint of the halogen ratios, brine generation through interaction with evaporates can be excluded.

The Rb/Cs ratio of a fluid is a sensitive pathway tracer (Burisch et al., 2016; Müller, Jacquemyn, et al., 2022; Müller, Walter, et al., 2022; Walter et al., 2018). Rb/Cs values about >2 indicate interaction with a claystone or clay minerals, which is the dominant process in the basin strata (7.4–17.9). This fits with the observation of oil shales and organic-rich claystones (FA7 and FA8, Figure 6O,P) near the B-rich interval. Rb/Cs values below 2 are related to clay mineral formation in basement rocks under hydrothermal conditions (50–150°C), which is not the case in the Ibar Basin (Burisch et al., 2016; Göb et al., 2013). Hence, a significant influence of fluids from the basement below the sediments is rather unlikely. This interpretation is also supported by the very low Mg and Ca contents in the fluids, which are unlikely for basement equilibrated fluids (Bucher & Stober, 2010; Frape & Fritz, 1987; Moeller et al., 1997; Stober & Bucher, 2004, 2005; Walter et al., 2017). Since albite is usually the alteration product in crystalline basement granites and gneisses (Jungmann et al., 2025; Walter et al., 2019), the Ca component becomes released into the fluids, which is not the case in the analysed samples in the Ibar Basin. The ophiolitic basement would release Mg, which was not dominant in the studied brine, while the Mg-rich brines were clearly active in the stratigraphically older units (Figure 2) being

responsible for the formation of magnesite hydrothermal-sedimentary deposit, Bela Stena (Falick et al., 1991).

Moreover, very low Li contents in the fluid indicate decoupling of the boron in the Ibar Basin, while in other intramontane basins (such as Valjevo-Mionica, Jadar, Borojević-Šošarić and Benko, 2023), this is not the case. Higher lithium contents would be expected in a remaining fluid if the responsible fluid is precipitated Li under equilibrium conditions (Burisch et al., 2016; Jungmann et al., 2025; Walter et al., 2019).

The observed mineral textures (Figures 9 and 10) show an evolution from Ca-borate (colemanite) to Ca-Na-borate (ulexite) to Na-borate (borax), which correlates with the evolution of the bittern brine. The same mineralogical evolution, from colemanite-dominated to ulexite-dominated lithologies, is identified as lateral and vertical zonation in other boron deposits (Bigadic deposit, western Anatolia; Loma Blanca, Puna region) at a macroscale (Alonso et al., 1988; Palmer & Helvacı, 1995).

Moreover, the fluid data indicate a significant Na enrichment of at least one log unit concentration from early to late colemanite formation that explains a successive supersaturation of Na-bearing boron minerals like ulexite and borax. However, no fluid data are available (due to grain-size restrictions) for ulexite and borax, which would finally prove the brine evolution. Moreover, the evolution of Fe-hydroxides in microbialite calcite I to pyrite in assemblage with ulexite and borax implies a shift in oxygen fugacity to more reduced conditions. The observation of hydrocarbons (and oil drops) in microbialite reduced conditions during deposit formation (Novaković et al., 2024).

By application of the activity diagrams of Birsoy and Özbaş (2012), the mineralogical evolution in the Ibar Basin is related to an increase in evaporation and a decrease in pH, controlling the transition from the colemanite to ulexite and, finally, to the borax stability field (Figure 14).

The aforementioned phase boundaries depend on the $B(OH)_3$ activity and are limited to $\log aB(OH)_3$ below 0–1. Based on the qualitative data of this contribution, it is not possible to provide evidence for (arrow B in Figure 14A) or against a shift in $B(OH)_3$ activity (arrow A in Figure 14A) or a combination of both. As the most reliable process is a decrease in $B(OH)_3$ activity with increasing evaporation, a combination of arrow A and arrow B in Figure 14A is most likely. Moreover, increased H_2O activity with increasing evaporation and decreasing pH is required to explain the observed paragenesis (Figure 14B).

5.4 | Climatic, tectonic and hydrothermal fluid flow controls on sedimentation in the Ibar Basin saline-alkaline lake

The results presented in this work allow for the definition of depositional events, the constraint of fluid flow evolution and the association of this with regional tectonic and climatic conditions. Finally, these new data can be used to propose a new model for saline-alkaline lake evolution in tectonically active regions.

Lake stages show lake expansion and evolution from fresh and open to hydrologically closed stratified saline lake (Figure 15). Based on our new age constraints of sedimentation that occurred during closed stratified saline lake (17 ± 0.43 Ma, Figure 8A), the basin evolution overlaps with the oldest extensional phase in the region (~ 21 – 17 Ma, Schefer et al., 2011). The extension drove the exhumation of metamorphic core complexes Studenica and Kopaonik. Their exhumation created a local source area supplying clastic sediments into the basin by alluvial fans at first and by deltas as the lake expanded (Figure 15A). The overall transgression and

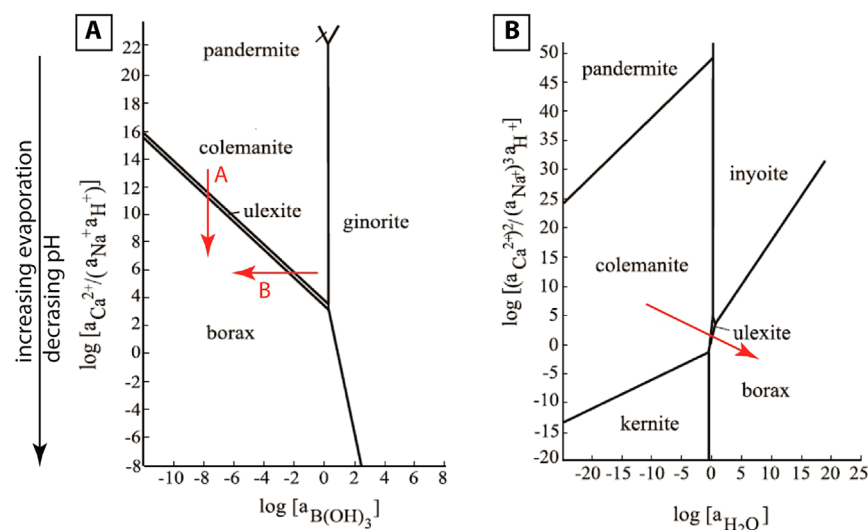


FIGURE 14 Phase diagrams adopted from Birsoy and Özbaş (2012). Red arrows indicate the qualitative evolution of the boron phase in the relationship of various parameters.

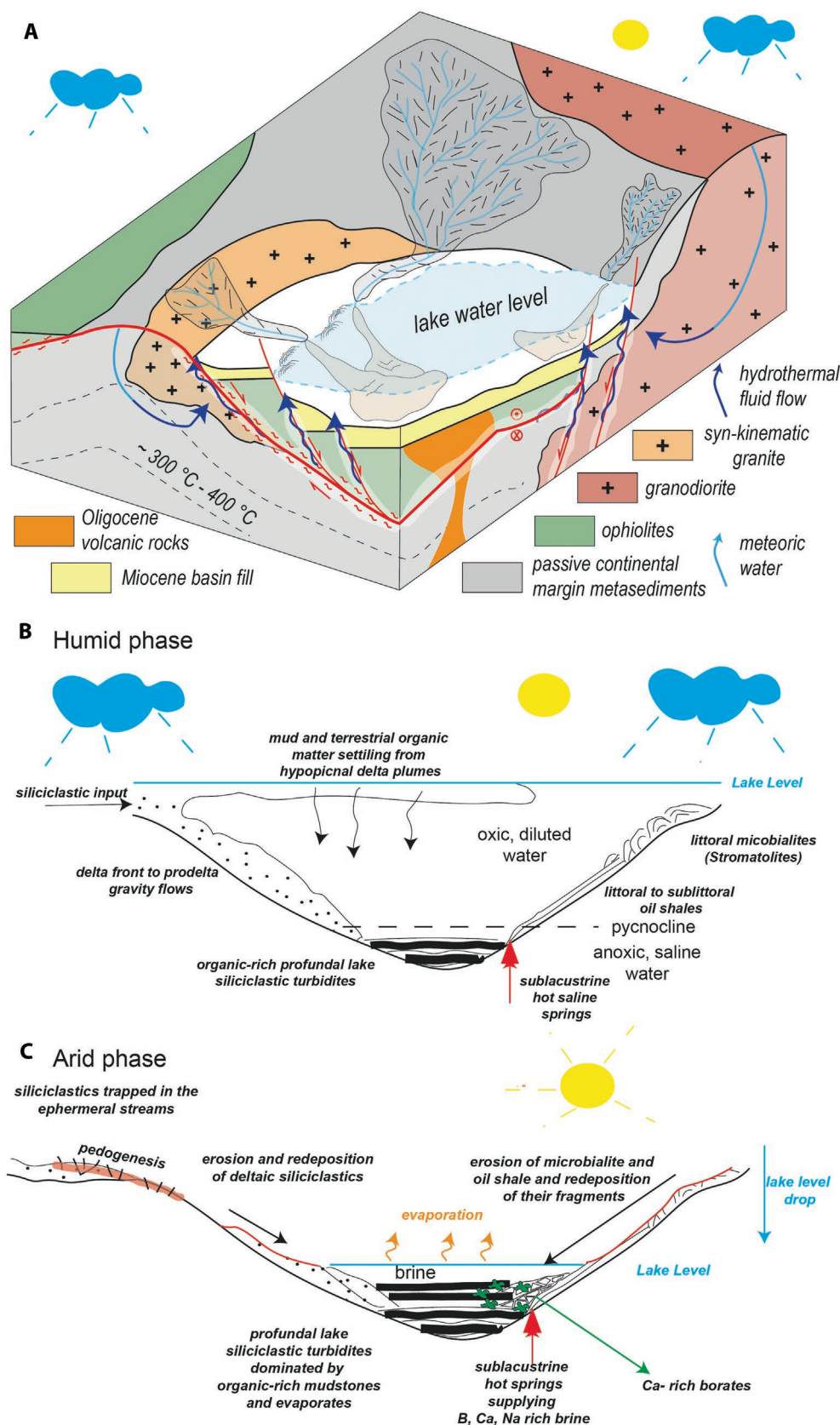


FIGURE 15 Depositional model of the studied stratigraphic section in Ibar Basin. (A) Regional extension controlling the accommodation space and hydrothermal fluid flow. Deposition in the hydrologically closed stratified lakes stage during (B) humid and (C) arid periods.

lake expansion and subsequent restriction are coeval with the global warm and humid Middle MCO (Zachos, 2011). However, quickly after its expansion, the lake becomes hydrologically closed, stratified and saline. Their depositional trends imply an increased seasonality. The humid periods are characterised by high water discharge and sediment supply by deltaic systems along the basin margin (Figure 15B). The increase in lake level and diluted water create favourable conditions for microbial activity, resulting in stromatolites on the protected lake littoral (Renaut et al., 2013). The arid periods are characterised by the retrogradational trend and are dominated by organic-rich profundal facies associations associated with the borates (Figure 15B). The ephemeral flows likely did not have the power to transport clastic sediments deeper into the basin. In the profundal, the lake level drop due to aridity is recorded by the basin-wide intrabasinal brecciation event induced by erosion. The youngest brecciation event is slightly younger than 17.13 ± 0.43 Ma, following new U–Pb dating. Considering its correlation with the regional extensional phase, the contribution of tectonics cannot be excluded. During the low lake level due to the arid phase, Ca^{2+} is removed from the drainage system by the formation of subsurface cements and calcrete in the drainage basin and through other fractionation processes (Renaut & Owen, 2023). This, together with higher salinity and shallowing of the water, reduces stromatolite development. In contrast, the precipitating syn-depositional borates (disseminated and nodular colemanite) are Ca rich, which poses a question of the origin of the high Ca in the system. The post-depositional colemanite associated with the faults and fissures cross-cutting the deepest parts of the studied borehole (Figure 9G,H) demonstrated that these faults were active and acted as a conduits for the delivery of the boron-rich brine into the basin. During ascent, the fluids invaded porous lithologies before the brine reached the lake bottom. The arid climatic conditions favoured brine saturation and borate precipitation on the muddy lake bottom or within the pores of brecciated profundal facies. Boron-rich brines likely accumulated at the lake bottom topographic lows due to their higher density compared to ambient water. Heavier boron-rich brines displaced the sediment pore waters at the sediment–water interface, precipitating Ca borates (Smith & Medrano, 1996). Ca-rich borate precipitated directly from the brine under redox conditions and grew within the unconsolidated fine-grained and clay mineral-rich sediment as it was compacted. As the Ca borate precipitation progressed, the system became relatively depleted in Ca^{2+} and enriched in Na^+ . It is likely residual Na enrichment; however, the effect of external Na-rich fluids cannot be excluded. Furthermore, due to compaction,

dewatering of the clay minerals leads to freshening of the system and provides H_2O activity. This affects the bittern brine evolution, leading to secondary Na-rich borates, that is ulexite and borax (Figures 10 and 14B). This process is associated with an increase in evaporation and a decrease in pH (Figure 14). It is likely that the subsequent Ca, B-rich brine inflow into the system led to an increase of Ca^{2+} in the system, favouring precipitation of colemanite. This study demonstrated that the circulation of the B-rich basinal brines and deposition of borates and calcite within the microbialite pore space and fractures lasted from ~17 to ~2 Ma (Figure 14B,C).

Following previous studies, there are two possible mechanisms providing B and Ca into the Ibar Basin (e.g. Alonso, 1999; Tanner et al., 2002; Zhang et al., 2022). Firstly is the weathering of volcanics and subsequently transport of B and Ca into the basin by surface run-off and shallow groundwater. The fact that some B-rich saline lakes (e.g. La Puna region, Alonso, 1999) are associated with a non-volcanic bedrock implies that weathering of volcanics might not play a crucial role as a B source.

The second possibility for the origin of B and Ca includes the leaching of the bedrock in the region (vulcanite, granite, granodiorites) in contact with deep-seated fluids or heated meteoric fluids transported via thermal springs (Figure 15A). Andrić et al. (2015) showed that the Ibar Basin developed in the region affected by a high geothermal gradient as a consequence of magmatic and metamorphic processes associated with the exhumation of the metamorphic rocks from mid-crustal levels (8–10 km, Schefer et al., 2011). This change in crustal isotherms affected the migration of hydrothermal fluids (basement-derived deep-seated and/or sediment-derived shallow and/or meteoric-derived water), which recharged the basin directly or fed streams in their discharge areas (examples in Uganda, Kenya and Ethiopia; Arad & Morton, 1969; Gizaw, 1996; Schagerl & Renaut, 2016; Searles Lake in the USA, Lowenstein et al., 2017; La Puna region, Andes, Alonso, 1999; Puga Valley, Kashmir, Garrett, 1998).

On their way to the basin, the hydrothermal fluids likely leach elements from the bedrock (volcanic, granite, granodiorites) and mobilise Ca, Na, B, HCO_3 , and other ions and compounds. The stratigraphically lower Mg deposit Bela Stena demonstrates that a similar system was active at an earlier stage of basin evolution, where Mg was leached from ophiolites (Falick et al., 1991). This implies that the exhumation of the metamorphic core and associated processes (Figure 15A) played an important role not only in generating basin accommodation space but also as a trigger for mobilising and transporting elements into the basin by providing heat

and perhaps deep fluids, as also observed in other regions such as the Tauern Window (Alps) and Cyclades (Neubauer, 2005).

The syndepositional borate accumulations are mainly associated with the hydrologically closed stratified stage of the basin, similar to the boron accumulations in western Anatolia, Nevada, California, Tibet and the Andes (e.g. Garrett, 1998; Helvacı & Alonso, 2000; Swihart et al., 1996). This suggests that the dry climatic phases and evaporation were important for the basinal brine to be sufficiently saturated. The semi-arid to arid climatic conditions in general included frequent and longer arid phases, which probably affected the internal Dinarides during Early to Middle Miocene times. Andrić-Tomašević et al. (2021) suggested that even though the MCO (Zachos et al., 2001) was a globally humid period, in the internal Dinarides the rain shadow effect of the Dinarides controlled an arid phase. This study supports this hypothesis and demonstrates local aridity in the south-eastern Europe which deviates from the generally humid trend during MCO. However, alkaline-saline lakes have been observed in other regions affected by rain shadow, such as the East African Rift (Renaut & Owen, 2023), but these are lacking B, Ca-rich deposits. This implies that convergence boundaries, collisional and accretionary types of orogens (such as Andes, Dinarides, North American Cordillera) are important tectonic settings as these include processes leading to highly evolved crustal melts where boron as an incompatible element is common. The structural reorganisations allowing exhumation of the B-enriched crustal material (e.g. Andrić, Vogt, et al., 2018; Cawood et al., 2009; DeCelles et al., 2009; Weller et al., 2021) and intramountain basins formation play an important role in mobilisation of B, Ca and their transport into the saline lakes. Certainly, their hydrological regime, a closed lake associated with arid climatic conditions, is central for the deposition and preservation of the B, Ca-rich units.

6 | CONCLUSIONS

The sedimentological, petrographic and geochemical characteristics of the studied sediments imply that the saline-alkaline lake of Ibar Basin evolved during the Early to Middle Miocene time. The lake evolution includes open and closed stratified lake stages. During the open lake stage, the humid climate of MCO, together with tectonic activity, controlled the high sediment supply into the lake. The sediments stored in alluvial and deltaic environments imply local sources derived from ophiolite, andesite and granodiorites. The change to more arid climate conditions led to a closed lake stage. It is characterised by lake level drops and negative water balance recorded by basin-wide

brecciated littoral to sublittoral facies associations (microbialites, oil shales), oil shales, marginal lake mudstones and sandstones, organic-rich profundal lake siliciclastics and borates dominated by colemanite. Likely, the shorter humid periods were marked by high discharge, supplying the basin with clastic sediment. Oxygenated, shallow lake areas outside clastic input fostered stromatolite evolution.

The new depositional U–Pb ages imply that the basin accommodation space was controlled by a regional extensional phase affecting the internal Dinarides and also influencing the elevation of the high geothermal gradient. This leads to the circulation of hydrothermal fluid flow (basement-derived deep-seated and/or sediment-derived shallow and/or meteoric-derived water), which eventually recharged the basin.

The progressive evaporation associated with a regional semi-arid climate led to the concentration of boron and its precipitation coeval with the deposition. The initially high $\text{Ca}^{2+}/\text{Na}^{+}$ ratio in the brine favoured the precipitation of colemanite. Ultimately, with the depletion of Ca^{2+} and breakdown of clays, Na–Ca and Na-rich borates were deposited (ulexite and borax). The clay mineral breakdown led to fluctuations in the salinity and hence stability fields of the boron minerals in the study area. In contrast to the numerous deposits where this transition is represented as zoning of the borate-rich succession, in Ibar Basin it is represented as an evolution of the bittern brine. This study emphasised the importance of the interplay of tectonic and magmatic processes within the collisional orogen, arid climate and basin hydrology in the evolution of B, Ca-rich depositional sequence and evolution of saline-alkaline lakes. However, further research on age dating, fluid properties and detailed textural relationships is required to build up a holistic model for boron mineralisation in various settings for which this study provides first insights.

ACKNOWLEDGEMENTS

N. Andrić-Tomašević was supported by the start-up research fund from the Karlsruhe Institute of Technology. The U–Pb dating was supported by the German Science Foundation (DFG DRASTIC project TO 1364 3-1 and INST 121384/213-1 FUGG). V. Simić and D. Životić's research was supported by the Ministry of Science, Technological Development and Innovation, Republic of Serbia (contract 451-03-47/2023-01/200126 and 451-03-66/2024-03/200052). A. Gerdes would like to acknowledge this as FIERCE contribution No. 200. We thankfully acknowledge Claudia Mössner and Maya Denker (all LERA staff) for helping with the crush leach analyses. Moreover, Elisabeth Eiche (LERA) is acknowledged for coordinating the lab work. We thankfully acknowledge Vojka Gardić and Dr. Renata Kovačević for

helping with the ICP-MS analyses. We thank Balkan Gold d.o.o. and RKU Ibarski Rudnici uglja for providing access to the samples and boreholes. NAT, JK, VS and DŽ provided funding. We gratefully acknowledge the helpful reviews of Ramon Mercedes-Martín, Michael Smith and the Anonymous reviewer that significantly improved the initial manuscript. Open Access funding enabled and organized by Projekt DEAL.

CONFLICT OF INTEREST STATEMENT

The authors declare no conflicts of interest.

DATA AVAILABILITY STATEMENT

All data are available in the supplementary materials.

ORCID

Nevena Andrić-Tomašević  <https://orcid.org/0000-0002-4325-6327>

Dragana Životić  <https://orcid.org/0000-0001-6218-7091>

REFERENCES

- Alonso, R.N. (1999) On the origin of La Puna Borates. *Acta Geologica Hispánica*, 34(2-3), 141–166.
- Alonso, R., Helvacı, C., Sureda, R. & Viramonte, J. (1988) A new tertiary Borax deposit in the Andes. *Mineralium Deposita*, 23, 299–305.
- Andelković, M., Eremija, M., Pavlović, M., Andelković, J. & Mitrović-Petrović, J. (1991) In: Andelković, M. (Ed.) *Paleogeography of serbia-tertiary*. Belgrade, Serbia: University of Belgrade, Faculty of Mining and Geology, Institute for Regional Geology and Paleontology, p. 237pp (in Serbian with English summary).
- Andrić, N., Fügenschuh, B., Životić, D. & Cvetković, V. (2015) The thermal history of the Miocene Ibar Basin (Southern Serbia): new constraints from fission track and vitrinite reflectance data. *Geologica Carpathica*, 66, 37–50.
- Andrić, N., Matenco, L., Hilgen, F. & de Bresser, H. (2018) Structural controls on sedimentation during asymmetric extension: the case of Sorbas Basin (SE Spain), Global Planet. *Change*, 171, 185–206.
- Andrić, N., Sant, K., Mačenco, L., Mandić, O., Tomljenović, B., Pavelić, D., Hrvatović, H., Demir, V. & Ooms, J. (2017) The link between tectonics and sedimentation in asymmetric extensional basins—inferences from the study of the Sarajevo-Zenica Basin. *Marine and Petroleum Geology*, 83, 305–332.
- Andrić, N., Vogt, K., Matenco, L., Cvetković, V., Cloetingh, S. & Gerya, T. (2018) Variability of orogenic magmatism during Mediterranean-style continental collisions: a numerical modelling approach. *Gondwana Research*, 56, 119–134. <https://doi.org/10.1016/j.jgr.2017.12.007>
- Andrić-Tomašević, N., Simić, V., Mandić, O., Životić, D., Suárez, M. & García-Romero, E. (2021) An arid phase in the Internal Dinarides during the early to middle Miocene: inferences from Mg-clays in the Pranjani Basin (Serbia). *Palaeogeography, Palaeoclimatology, Palaeoecology*, 562, 110–145. <https://doi.org/10.1016/j.palaeo.2020.110145>
- Andrić-Tomašević, N., Simić, V., Životić, D., Nikolić, N., Pavlović, A., Kluge, T., Beranoaguirre, A., Smit, J. & Bechtel, A. (2024) Tectonically induced travertine deposition in the Levač intramontane basin (Central Serbia). *Sedimentology*, 71, 1214–1244. <https://doi.org/10.1111/sed.13171>
- Arad, A. & Morton, W.H. (1969) Mineral springs and saline lakes of the Western Rift Valley, Uganda. *Geochimica et Cosmochimica Acta*, 33, 1169–1181.
- Bentham, P.A., Talling, P.J. & Burbank, D.W. (1993) Braided stream and flood-plain deposition in a rapidly aggrading basin: the Escanilla formation, Spanish Pyrenees. *Geological Society of London, Special Publication*, 75, 177–194.
- Beranoaguirre, A., Vasiliev, I. & Gerdes, A. (2022) In situ LA-ICPMS U–Pb dating of sulfates: applicability of carbonate reference materials as matrix-matched standards. *Geochronology*, 4, 601–616. <https://doi.org/10.5194/gchron-4-601-2022>
- Birsoy, R. & Özbaş, Ü. (2012) Activity diagrams of borates: implications on common deposits. *Carbonates and Evaporites*, 27, 71–85. <https://doi.org/10.1007/s13146-012-0085-6>
- Blair, T.C. & McPherson, J.G. (1994) Alluvial fans and their natural distinction from rivers based on morphology, hydraulic processes, sedimentary processes, and facies assemblages. *Journal of Sedimentary Research*, 64, 450–489.
- Bohacs, K.M., Carroll, A.R., Neal, J.E. & Mankiewicz, P.J. (2000) Lake-basintype, source potential, and hydrocarbon character: An integrated sequence-stratigraphic–geochemical framework. In: Gierlowski-Kordesch, E. & Kelts, K. (Eds.) *Lake basins through space and time: American association of petroleum geologists studies in Geology*, Vol. 46. Boulder, Tulsa, pp. 3–37.
- Bons, P.D., Fusswinkel, T., Gomez-Rivas, E., Markl, G., Wagner, T. & Walter, B. (2014) Fluid mixing from below in unconformity-related hydrothermal ore deposits. *Geology*, 42(12), 1035–1038. <https://doi.org/10.1130/G35708.1>
- Borojević-Šošarić, S., Cvetković, V., Neubauer, F., Palinkaš, L., Bernroider, M. & Genser, J. (2012) Oligocene shoshonitic rocks of the Rogozna Mts. (Central Balkan Peninsula): Evidence of petrogenetic links to the formation of Pb–Zn–Ag ore deposits. *Lithos*, 148, 176–195. <https://doi.org/10.1016/j.lithos.2012.05.028>
- Bouma, A.H., Kuenen, P.H. & Shepard, F.P. (1962) *Sedimentology of some flysch deposits: a graphic approach to facies interpretation*, Vol. 168. Amsterdam: Elsevier.
- Brković, T., Malešević, M., Urošević, M., Trifunović, S. & Radanović, Z. (1976) Basic Geological Map of the SFRY, 1:100.000, Sheet Ivanjica (K34–17). Federal Geological Institute of Yugoslavia. Belgrade (in Serbian).
- Bucher, K. & Stober, I. (2010) Fluids in the upper continental crust. *Geofluids*, 10, 241–253. <https://doi.org/10.1111/j.1468-8123.2010.00279.x>
- Bull, S., Cartwright, J. & Huuse, M. (2009) A subsurface evacuation model for submarine slope failure. *Basin Research*, 21, 433–443.
- Burisch, M., Marks, M.A., Nowak, M. & Markl, G. (2016) The effect of temperature and cataclastic deformation on the composition of upper crustal fluids—an experimental approach. *Chemical Geology*, 433, 24–35.
- Cao, J., Wu, M., Chan, Y., Hu, K., Bian, L.Z., Wang, L.G. & Zhang, Y. (2012) Trace and rare earth elements geochemistry of Jurassic mudstones in the northern Qaidam basin, north-west China. *Chemie der Erde-Geochemistry*, 72, 245–252.
- Carroll, A.R. & Bohacs, K.M. (1999) Stratigraphic classification of ancient lakes: balancing tectonic and climatic controls. *Geology*, 27, 99–102.
- Cawood, P.A., Kröner, A., Collins, W.J., Kusky, T.M., Mooney, W.D. & Windley, B.F. (2009) Windley Accretionary orogens through

- Earth history. *Geological Society, London, Special Publications*, 318, 1–36. <https://doi.org/10.1144/SP318.1>
- Cohen, A., McGlue, M.M., Ellis, G.S., Zani, H., Swarzenski, P.W., Assine, M.L. & Silva, A. (2015) Lake formation, characteristics, and evolution in retroarc deposystems: a synthesis of the modern Andean orogen and its associated basins. In: DeCelles, P.G., Ducea, M.N., Carrapa, B. & Kapp, P.A. (Eds.) *Geodynamics of a Cordilleran Orogenic System: the Central Andes of Argentina and Northern Chile*, Vol. 212. Boulder, Colorado: Geological Society of America Memoir, pp. 309–335. [https://doi.org/10.1130/2015.1212\(16\)](https://doi.org/10.1130/2015.1212(16))
- Cohen, A.S., Lezzar, K.-E., Tiercelin, J.-J. & Soreghan, M. (1997) New palaeogeographic and lake-level reconstructions of Lake Tanganyika: implications for tectonic, climatic and biological evolution in a rift lake. *Basin Research*, 9, 107–132. <https://doi.org/10.1046/j.1365-2117.1997.00038.x>
- Cvetković, V. (2002) Nature and origin of pyroclastic deposits of the Miocene Eruptive Complex of Borač (Central Serbia). *Bulletin, Classe des Sciences Mathématiques et Naturelles, Sciences mathématiques Académie Serbe des Sciences et des Arts, Beograd*, 342, 209–215.
- Cvetković, V., Karamata, S. & Knežević-Đorvević, V. (1995) Volcanic rock of the Kopaonik area. [Savetovanje “Geologija i metalogenija Kopaonika”]. Republički društveni fond za geološka istraživanja Srbije, 19–22 June, 185–195 (in Serbian with English abstract).
- Cvetković, V. & Pécskay, Z. (1999) The Early Miocene eruptive complex of Borač (central Serbia): volcanic facies and evolution over time. Extended abstract. *Carpathian Geology 2000*, October 11–14, 1999, Smolenice, Geol. *Carpathica*, 50, 91–93.
- Cvetković, V., Pécskay, Z. & Šarić, K. (2013) Cenozoic igneous tectonomagmatic events in the Serbian part of the Balkan Peninsula: inferences from K/Ar geochronology. *Acta Volcanologica*, 10, 111–120.
- Cvetković, V., Prelević, D., Downes, H., Jovanović, M., Vaselli, O. & Pécskay, Z. (2004) Origin and geodynamic significance of Tertiary postcollisional basaltic magmatism in Serbia (Central Balkan Peninsula). *Lithos*, 73, 161–186.
- de Leeuw, A., Mandić, O., Krijgsman, W., Kuiper, K. & Hrvatić, H. (2012) Paleomagnetic and geochronologic constraints on the geodynamic evolution of the Central Dinarides. *Tectonophysics*, 530–531, 286–298.
- de Leeuw, A., Mandić, O., Krijgsman, W., Kuiper, K.F. & Hrvatić, H. (2011) A chronostratigraphy for the Dinaride Lake System deposits of the Livno-Tomislavgrad Basin: the rise and fall of a long-lived lacustrine environment. *Newsletters on Stratigraphy*, 8, 29–43.
- DeCelles, P.G., Ducea, M.N., Kapp, P. & Zandt, G. (2009) Cyclicity in Cordilleran orogenic systems. *Nature Geoscience*, 2, 251–257.
- DeCelles, P.G., Gray, M.B., Ridgway, K.D., Cole, R.B., Pivnik, D.A., Pequera, N. & Srivastava, P. (1991) Controls on synorogenic alluvial-fan architecture, Beartooth Conglomerate (Palaeocene). *Wyoming and Montana Sedimentology*, 38(4), 567–590.
- Deocampo, D.M. & Jones, B.F. (2014) Geochemistry of saline lakes. In: Drever, J.I. (Ed.) *Treatise on geochemistry volume 7: surface and groundwater, weathering, and soils*. Amsterdam: Elsevier, pp. 437–469.
- Diloreto, Z.A., Garg, S., Bontognali, T.R.R. & Dittrich, M. (2021) Modern dolomite formation caused by seasonal cycling of oxygenic phototrophs and anoxygenic phototrophs in a hypersaline sabkha. *Scientific Reports*, 11, 4170. <https://doi.org/10.1038/s41598-021-83676-1>
- Dimitrijević, M.D. (1997) *Geology of Yugoslavia*, 2nd edition. Belgrade: Geoinstitute, pp. 1–187.
- Epp, T., Walter, B.F., Scharrer, M., Lehmann, G., Henze, K., Heimgärtner, C., Bach, W. & Markl, G. (2019) Quartz veins with associated Sb-Pb-Ag±Au mineralization in the Schwarzwald, SW Germany: a record of metamorphic cooling, tectonic rifting, and element remobilization processes in the Variscan belt. *Mineralium Deposita*, 54, 281–306.
- Erak, D., Matenco, L., Toljić, M., Stojadinović, U., Andriessen, P.A., Willingshofer, E. & Ducea, M.N. (2017) From nappe stacking to extensional detachments at the contact between the Carpathians and Dinarides—The Jastrebac Mountains of Central Serbia. *Tectonophysics*, 710, 162–183.
- Ercegovac, M., Wolf, M., Hagemann, H.W. & Püttmann, W. (1991) Petrological and geochemical studies of the coals of the Ibar River basin (Yugoslavia). *International Journal of Coal Geology*, 19, 145–162 (in German).
- Eugster, H.P. & Jones, B.F. (1968) Gels composed of sodium-aluminum silicate, Lake Magadi, Kenya. *Science*, 161, 160–163.
- Falick, A.E., Ilić, M. & Russel, M.J. (1991) A stable isotope study of the magnesite deposits associated with the alpine-type ultramafic rocks of Yugoslavia. *Economic Geology*, 86, 847–861.
- Fodor, L., Bada, G., Csillag, G., Horváth, E., Ruszkiczay-Rudiger, Z., Palotas, K., Sikhegyi, F., Timar, G. & Cloetingh, S. (2005) An outline of neotectonic structures and morphotectonics of the western and central Pannonian Basin. *Tectonophysics*, 410, 15–41. <https://doi.org/10.1016/j.tecto.2005.06.008>
- Frape, S.K. & Fritz, P. (1987) Geochemical trends for groundwaters from the Canadian Shield. In: Frit, P. & Frape, S.K. (Eds.) *Saline water and gases in crystalline rocks*, Vol. 33. Canada, Toronto: Geological Association of Canada, pp. 19–38.
- Fu, X., Wang, J., Chen, W., Feng, X., Wang, D., Song, C. & Zeng, S. (2016) Elemental geochemistry of the early Jurassic black shales in the Qiangtang Basin, eastern Tethys: constraints for paleoenvironment conditions. *Journal of Geology*, 51, 443–454.
- Gagic, N. (1985) Micropaleontologic analysis of the Miocenes sediments of the Bella Stena deposit, Fondovski Miaterijal [Beograd], v. 3, pp. 11–15 (in Serbian), Belgrade, Serbia.
- García-García, F., Fernández, J., Viseras, C. & Soria, J.M. (2006) Architecture and sedimentary facies evolution in a delta stack controlled by fault growth (Betic Cordillera, southern Spain, late Tortonian). *Sedimentary Geology*, 185, 79–92.
- Garrett, D.E. (1998) *Borates: handbook of deposits, processing, properties, and use*. San Diego, California: Academic Press.
- Gee, M.J.R., Masson, D.G., Watts, A.B. & Allen, P.A. (1999) The Saharan debris flow: an insight into the mechanics of long runout submarine debris flows. *Sedimentology*, 46, 315–335.
- Gerdes, A. & Zeh, A. (2006) Combined U-Pb and Hf isotope LA-(MC)-ICP-MS analyses of detrital zircons: comparison with SHRIMP and new constraints for the provenance and age of an Armorican metasediment in Central Germany. *Earth and Planetary Science Letters*, 249, 47–61. <https://doi.org/10.1016/j.epsl.2006.06.039>
- Gerdes, A. & Zeh, A. (2009) Zircon formation versus zircon alteration—new insights from combined U-Pb and Lu-Hf in-situ LA-ICP-MS analyses, and consequences for the interpretation of Archean zircon from the Central Zone of the Limpopo Belt.

- Chemical Geology*, 261(3–4), 230–243. <https://doi.org/10.1016/j.chemgeo.2008.03.005>
- Gierlowski-Kordesch, E.H. & Rust, B.R. (1994) The Jurassic East Berlin Formation, Hartford basin, Newark Supergroup (Connecticut and Massachusetts): a saline lake-playa-alluvial plain system. In: Renaut, R.W. & Last, W.M. (Eds.) *Sedimentology and geochemistry of modern and ancient saline lakes*, Vol. 50. Claremore: SEPM Special Publications, pp. 249–265.
- Gizaw, B. (1996) The origin of high bicarbonate and fluoride concentrations in waters of the Main Ethiopian Rift Valley, East African Rift system. *Journal of African Earth Sciences*, 22, 391–402.
- Göb, S., Loges, N., Nolde, M., Bau, D.E. & Jacob, G.M. (2013) Major and trace element compositions (including REE) of mineral, thermal, mine and surface waters in SW Germany and implications for water–rock interaction. *Applied Geochemistry*, 33, 127–152.
- Goldstein, R.H. & Reynolds, T.J. (1994) *Systematics of fluid inclusions in diagenetic minerals, short course notes*, Vol. 31. Tulsa, USA: SEPM Society for Sedimentary Geology. <https://doi.org/10.2110/scn.94.31>
- Graf, J.W., Carroll, A.R. & Smith, M.E. (2015) Lacustrine sedimentology, stratigraphy and stable isotope geochemistry of the tipton member of the green river formation. In: Smith, M. & Carroll, A. (Eds.) *Stratigraphy and Paleolimnology of the Green River Formation, Western USA*, Syntheses in Limnogeology, Vol. 1. Dordrecht: Springer. https://doi.org/10.1007/978-94-017-9906-5_3
- Guillong, M., Wotzlaw, J.F., Looser, N. & Laurent, O. (2020) Evaluating the reliability of U–Pb laser ablation inductively coupled plasma mass spectrometry (LA–ICP–MS) carbonate geochronology: matrix issues and a potential calcite validation reference material. *Geochronology*, 2, 155–167. <https://doi.org/10.5194/gchron-2-155-2020>
- Guo, P., Wen, H., Li, C., He, H. & Sánchez-Román, M. (2023) Lacustrine dolomite in deep time: what really matters in early dolomite formation and accumulation? *Earth-Science Reviews*, 246, 104575. <https://doi.org/10.1016/j.earscirev.2023.104575>
- Helvacı, C. & Alonso, R.N. (2000) Borate deposits of Turkey and Argentina; a summary and geological comparison. *Turkish Journal of Earth Sciences*, 9, 1–27. <https://journals.tubitak.gov.tr/earth/vol9/iss1/1>
- Helvacı, C. & Ortı, F. (2004) Zoning in the Kırka borate deposit, western Turkey: primary evaporitic fractionation or diagenetic modifications? *The Canadian Mineralogist*, 42, 1179–1204. <https://doi.org/10.2113/gscanmin.42.4.1179>
- Hill, C.A., Polyak, V.J., Asmerom, Y. & Provenci, P.P. (2016) Constraints on a Late Cretaceous uplift, denudation, and incision of the Grand Canyon region, southwestern Colorado Plateau, USA, from U–Pb dating of lacustrine limestone. *Tectonics*, 35, 896–906. <https://doi.org/10.1002/2016TC004166>
- How, H. (1868) Contributions to the mineralogy of Nova Scotia. III. Borates and other minerals in anhydrite and gypsum. Silicoborocalcite, a new mineral. *Philosophical Magazine*, 35 (4th Ser.), 32–41: 218.
- Huc, J., Le Fournier, M. & Vandenbroucke, G. (1990) Bessereau Northern Lake Tanganyika—an example of organic sedimentation in an anoxic rift lake. In: Katz, B.J. (Ed.) *Lacustrine Basin Exploration: case studies and modern analogs*, Vol. 50. Tulsa: American Association of Petroleum Geologists, pp. 169–185.
- Ielpi, A. (2012) Anatomy of major coal successions: facies analysis and sequence architecture of a brown coal-bearing valley fill to lacustrine tract (Upper Valdarno Basin, Northern Apennines, Italy). *Sedimentary Geology*, 265, 163–181.
- Ilić, A. & Neubauer, F. (2005) Tertiary to recent oblique convergence and wrenching of the central dinarides: constraints from a palaeostress study. *Tectonophysics*, 410, 465–484.
- Jackson, A.W., Jr. (1884) On colemanite, a new borate of lime. *American Journal of Science*, 3rd series, 28, 447–448.
- Jochum, K.P., Weis, U., Stoll, B., Kuzmin, D., Yang, Q., Raczek, I., Jacob, D.E., Stracke, A., Birbaum, K., Frick, D.A., Günther, D. & Enzweiler, J. (2011) Determination of reference values for NIST SRM 610–617 glasses following ISO guidelines. *Geostandards and Geoanalytical Research*, 35, 97–429. <https://doi.org/10.1111/j.1751-908X.2011.00120.x>
- Jungmann, M., Walter, B.F., Eiche, E., Giebel, R.J. & Kolb, J. (2025) The source of lithium in connate fluids: evidence from the geothermal reservoir at Soultz-sous-Forêts, Upper Rhine Graben, France. *Journal of Geochemical Exploration*, 270, 107641.
- Karamata, S. (2006) The geological development of the Balkan Peninsula related to the approach, collision and compression of Gondwanan and Eurasian units. In: Robertson, A.H.F. & Mountrakis, D. (Eds.) *Tectonic development of the Eastern Mediterranean Region*, Vol. 260. London: Geological Society of London Special Publications, pp. 155–178.
- Karamata, S., Vasković, N., Cvetković, V. & Knežević, V. (1994) The Upper Cretaceous and Tertiary magmatics of the central and eastern Serbia and their metallogeny. *Annals of the Geological Society of the Balkan Peninsula*, 56(1), 263–283.
- Keim, M.F., Walter, B.F., Neumann, U., Kreissl, S., Bayerl, R. & Markl, G. (2019) Polyphase enrichment and redistribution processes in silver-rich mineral associations of the hydrothermal fluorite-barite-(Ag–Cu) Clara deposit, SW Germany. *Mineralium Deposita*, 54, 155–174.
- Kelts, K. & Hsü, K.J. (1978) Freshwater carbonate sedimentation. In: Lerman, A. (Ed.) *Lakes: chemistry, geology, physics*. New York: Springer, pp. 294–323.
- Ketris, M.P. & Yudovich, Y.A.E. (2009) Estimations of Clarkes for carbonaceous biolithes: world averages for trace element contents in black shales and coals. *International Journal of Coal Geology*, 78, 135–148.
- Kochansky, V. & Slisković, T. (1981) Jüngere Miozäne Kongerien in Kroatien, Bosnien und Herzegovina. *Palaeontologia Jugoslavica Zagreb*, 19, 1–98.
- Köhler, J., Schönenberger, J., Upton, B. & Markl, G. (2009) Halogen and trace-element chemistry in the Gardar Province, south Greenland: subduction-related mantle metasomatism and fluid exsolution from alkali melts. *Lithos*, 113, 731–747.
- Kolchugin, A., Immenhauser, A., Morozov, V., Walter, B., Eskin, A., Korolev, E. & Neuser, R. (2020) A comparative study of two Mississippian dolostone reservoirs in the Volga–Ural Basin, Russia. *Journal of Asian Earth Sciences*, 199, 104465.
- Kolchugin, A.N., Immenhauser, A., Walter, B.F. & Morozov, V.P. (2016) Diagenesis of the palaeo-oil-water transition zone in a Lower Pennsylvanian carbonate reservoir: constraints from cathodoluminescence microscopy, microthermometry, and isotope geochemistry. *Marine and Petroleum Geology*, 72, 45–61.
- Kreissl, S., Gerdes, A., Walter, B.F., Neumann, U., Wenzel, T. & Markl, G. (2018) Reconstruction of a >200 Ma multi-stage

- "five element" Bi-Co-Ni-Fe-As-S system in the Penninic Alps, Switzerland. *Ore Geology Reviews*, 95, 746–788.
- Krštić, N., Dumadzanov, N., Olujić, J., Vujanović, L. & Janković-Golubović, J. (2001) Interbedded tuff and bentonite in the Neogene lacustrine sediments of the central part of the Balkan Peninsula. A review. *Acta Vulcanologica*, 13, 91–99.
- Krštić, N., Savić, L., Jovanović, G. & Bodor, E. (2003) Lower Miocene lakes of the Balkan Land. *Acta Geologica Hungarica*, 46, 291–299.
- Ladenburger, S., Walter, B.F. & Marks, M.A. (2020) Combining ion chromatography and total reflection X-ray fluorescence for detection of major, minor and trace elements in quartz-hosted fluid inclusions. *Journal of Analytical Chemistry*, 75, 1477–1485. <https://doi.org/10.1134/S106193482011009X>
- Larsen, E.S. & Hicks, W.B. (1914) Searlesite, a new mineral. *American Journal of Science*, 38, 437–440.
- Longhitano, S.G., Sabato, L., Tropeano, M., Murru, M., Carannante, G., Simone, L., Cilona, A. & Vigorito, M. (2015) Outcrop reservoir analogous and porosity changes in continental deposits from an extensional basin: the case study of the upper Oligocene Sardinia Graben System, Italy. *Marine and Petroleum Geology*, 67, 439–459.
- Lowenstein, T.K., Jagniecki, E.A., Carroll, A.R., Smith, M.E., Renaut, R.W. & Owen, R.B. (2017) The Green River salt mystery: what was the source of the hyperalkaline lake waters? *Earth Science Reviews*, 173, 295–306.
- Lowenstein, T.L. & Lauren, A.C. (2016) Dolginko, Javier García-Veigas; Influence of magmatic-hydrothermal activity on brine evolution in closed basins: searles Lake, California. *GSA Bulletin*, 128(9–10), 1555–1568. <https://doi.org/10.1130/B31398.1>
- Ludwig, K.R. (2012) *User's manual for isoplot version 3.75–4.15: a geochronological toolkit for Microsoft excel*. Berkeley: Berkeley Geochronological Center Special Publication, p. 5.
- Mandic, O., Pavelic, D., Harzhauser, M., Zupanic, J., Reischenbacher, D., Sachsenhofer, R.F., Tadej, N. & Vranjkovic, A. (2009) Depositional history of the Miocene Lake Sinj (Dinaride Lake System, Croatia): a long-lived hard-water lake in a pull-apart tectonic setting. *Journal of Paleolimnology*, 41, 431–452.
- Matenco, L. & Radivojević, D. (2012) On the formation and evolution of the Pannonian Basin: constraints derived from the structure of the junction area between the Carpathians and Dinarides. *Tectonics*, 31, TC6007.
- McCarthy, P.J., Martini, I.P. & Leckie, D.A. (1997) Anatomy and evolution of a Lower Cretaceous alluvial plain: sedimentology and palaeosols in the upper Blairmore Group, south-western Alberta, Canada. *Sedimentology*, 44, 197–220.
- Melchor, R.N. (2007) Changing lake dynamics and sequence stratigraphy of syn-rift lacustrine strata in a half-graben: an example from the Triassic Ischigualasto-Villa Unión Basin, Argentina. *Sedimentology*, 54, 1417–1446.
- Miall, A.D. (1996) *The geology of fluvial deposits*. New York: Springer, p. 582.
- Mladenović, A., Trivić, B. & Cvetković, V. (2015) How tectonics controlled post-collisional magmatism within the Dinarides: inferences based on study of tectono-magmatic events in the Kopaonik Mts. (Southern Serbia). *Tectonophysics*, 646, 36–49.
- Moeller, P., Weise, S.M., Althaus, E., Bach, W., Behr, H.J., Borchardt, R., Bräuer, K., Drescher, J., Erzinger, J., Faber, E., Hansen, B.T., Horn, E.E., Huenges, E., Kämpf, H., Kessels, W., Kirsten, T., Landwehr, D., Lodemann, M., Machon, L., Pekdeger, A., Pielow, H.-U., Reutel, C., Simon, K., Walther, J. & Weinlich, F.H. (1997) Paleofluids and recent fluids in the upper continental crust: results from the German Continental Deep Drilling Program (KTB). *Journal of Geophysical Research: Solid Earth*, 102(B8), 18233–18254.
- Mojsilović, S., Baklajić, D. & Djoković, I. (1978) *Basic geological map of the SFRY, 1:100,000, Sheet Sjenica (K32-29)*. Belgrade: Federal Geological Institute.
- Mulder, T. & Alexander, J. (2001) Abrupt change in slope causes variation in the deposit thickness of concentrated particle-driven density currents. *Marine Geology*, 175(1), 221–235.
- Müller, M., Igbokwe, O.A., Walter, B., Pederson, C.L., Riechelmann, S., Richter, D.K. & Immenhauser, A. (2020) Testing the preservation potential of early diagenetic dolomites as geochemical archives. *Sedimentology*, 67(2), 849–881.
- Müller, M., Jacquemyn, C., Walter, B.F., Pederson, C.L., Schurr, S.L., Igbokwe, O.A., Jöns, N., Riechelmann, S., Dietzel, M., Strauss, H. & Immenhauser, A. (2022) Constraints on the preservation of proxy data in carbonate archives—lessons from a marine limestone to marble transect, Latemar, Italy. *Sedimentology*, 69(2), 423–460.
- Müller, M., Walter, B.F., Swart, P.K., Jöns, N., Jacquemyn, C., Igbokwe, O.A. & Immenhauser, A. (2022) A tale of three fluids: fluid-inclusion and carbonate clumped-isotope paleothermometry reveals complex dolomitization and dedolomitization history of the Latemar platform. *Journal of Sedimentary Research*, 92(12), 1141–1168.
- Muniz, D.C. & Bosence, D. (2018) Lacustrine carbonate platforms: facies, cycles, and tectonosedimentary models for the presalt Lagoa Feia Group (lower Cretaceous), Campos basin, Brazil. *AAPG Bulletin*, 102, 2569–2597.
- Nemec, W. & Postma, G. (1993) Quaternary alluvial fans in south-western Crete: sedimentation processes and geomorphic evolution. In: *Alluvial sedimentation*, Vol. 17. Gent, Belgium: IAS Special Publication, pp. 235–276.
- Neubauer, F. (2005) Structural control of mineralization in metamorphic core complexes, Mineral Deposit Research: meeting the Global Challenge, 2005.
- Nöllner, C. (1870) Über den Lüneburgit. *Sitzungsberichte der königlich bayerischen Akademie der Wissenschaften zu München, Band I*, 291–293.
- Novaković, Ž., Nikolić, N., Andrić-Tomašević, N., Gajić, V., Suárez, M., García-Romero, E., Simić, V. & Životić, D. (2024) Mineralogy, chemistry, and distribution of selected trace elements in coal and shale from the Ibar Basin (South Serbia). *Thermal Science*, 28(5), 4131–4151. <https://doi.org/10.2298/TSCI240405143N>
- Nuriel, P., Wotzlaw, J.F., Ovtcharova, M., Vaks, A., Stremtan, C., Šala, M., Roberts, N.M.W. & Kylander-Clark, A.R.C. (2021) The use of ASH-15 flowstone as a matrix-matched reference material for laser-ablation U–Pb geochronology of calcite. *Geochronology*, 3, 35–47. <https://doi.org/10.5194/gchron-3-35-2021>
- Obradović, J. (1983) Some aspects of the sedimentation in the Neogene lake basins in Serbia [abs.] Internat. Assoc Sedimentologists Mtg., 4th, Split, Yugoslavia April 1983, Abstracts, p. 18–20.
- Obradović, J., Đurđević-Colson, J. & Vasić, N. (1997) Phytogenic lacustrine sedimentation-oil shales in Neogene from Serbia, Yugoslavia. *Journal of Paleolimnology*, 18, 351–364.
- Obradović, J., Stamatakis, M.G., Anicic, S. & Economou, G.S. (1992) Borate and borosilicate deposits in the Miocene Jarandol

- Basin, Serbia, Yugoslavia. *Economic Geology*, 87(8), 2169–2174. <https://doi.org/10.2113/gsecongeo.87.8.2169>
- Obradović, J. & Vasić, N. (2007) Neogene lacustrine basins from Serbia (Jezerški baseni u neogenu Srbije). *Srpska akademija nauka i umetnosti, Posebna izdanja*, 662, 1–310 (In Serbian).
- Pagel, M., Bonifacie, M., Schneider, D.A., Gautheron, C., Brigaud, B., Calmels, D., Cros, A., Saint-Bezar, B., Landrein, P., Sutcliffe, C. & Davis, D. (2018) Improving paleohydrological and diagenetic reconstructions in calcite veins and breccia of a sedimentary basin by combining $\Delta 47$ temperature, $\delta 18\text{O}$ water and U-Pb age. *Chemical Geology*, 481, 1–17. <https://doi.org/10.1016/j.chemgeo.2017.12.026>
- Palmer, M. & Helvacı, C. (1995) The boron isotope geochemistry of the Kırka borate deposit, western Turkey. *Geochimica et Cosmochimica Acta*, 59, 3599–3605.
- Pamić, J., Tomljenović, B. & Balen, D. (2002) Geodynamic and petrogenetic evolution of Alpine ophiolites from the central and NW Dinarides: an overview. *Lithos*, 65, 113–142.
- Pietras, J.T. & Carroll, A.R. (2006) High-resolution stratigraphy of an underfilled lake basin: Wilkins Peak Member, Eocene Green River Formation, Wyoming, U.S.A. *Journal of Sedimentary Research*, 76, 1197–1214.
- Pietras, J.T., Carroll, A.R. & Rhodes, M.K. (2003) Lake basin response to tectonic drainage diversion, Eocene Green River Formation, Wyoming. *Journal of Paleolimnology*, 30, 115–125.
- Pisarska-Jamroz, M. & Weckwerth, P. (2013) Soft-sediment deformation structures in a Pleistocene glaciolacustrine delta and their implications for the recognition of subenvironments in delta deposits. *Sedimentology*, v 60, 637–665.
- Platt, N.H. & Wright, V.P. (1991) Lacustrine carbonates: facies models, facies distributions and hydrocarbon aspects. In: Anadón, P., Cabrera, L. & Kelts, K. (Eds.) *Lacustrine Facies Analysis*, Vol. 13. Gent, Belgium: International Association of Sedimentologists. Special Publication, pp. 57–74.
- Postma, G. (1990) An analysis of the variation in delta architecture. *Terra Nova*, 2(2), 124–130.
- Postma, G. & Drinia, H. (1993) Architecture and sedimentary facies evolution of a marine, expanding outer-arc half-graben (Crete, late Miocene). *Basin Research*, 5(2), 103–124.
- Pryszajhnjuk, V., Kovalenko, V. & Krstić, N. (2000) On the terrestrial and freshwater molluscs from Neogene of Western Serbia. Geology and metallogeny of the Dinarides and the Vardar zone. Proc. Internat. Symp., Zvornik, Belgrade, 219–224.
- Renaut, R.W. & Gierlowski-Kordesch, E.H. (2010) Lakes. In: James, N.P. & Dalrymple, R.W. (Eds.) *Facies models*, Vol. 6. Canada: Geological Association of Canada, IV Series, GEOtext, pp. 541–575.
- Renaut, R.W., Owen, R.B., Jones, B., Tiercelin, J.-J., Tarits, C., Ego, J.K. & Konhauser, K.O. (2013) Impact of lake-level changes on the formation of thermogene travertine in continental rifts: Evidence from Lake Bogoria, Kenya Rift Valley. *Sedimentology*, 60, 428–468.
- Renaut, R.W. & Owen, R.B. (2023) *The Kenya Rift lakes: modern and ancient*. Berlin, Heidelberg: Springer, p. 977.
- Renaut, R.W., Owen, R.B., Lowenstein, T.K., De Cort, G., McNulty, E., Scott, J.J. & Mbuthia, A. (2021) The role of hydrothermal fluids in sedimentation in saline alkaline lakes: evidence from Nasikie Engida, Kenya Rift Valley. *Sedimentology*, 68, 108–134. <https://doi.org/10.1111/sed.12778>
- Rhodes, M.K. & Carroll, A.R. (2015) Lake type transition from balanced-fill to overfilled: laney member, Green River Formation, Washakie Basin, Wyoming. In: Smith, M. & Carroll, A. (Eds.) *Stratigraphy and paleolimnology of the Green River Formation, Western USA*, Syntheses in Limnogeology, Vol. 1. Dordrecht: Springer. https://doi.org/10.1007/978-94-017-9906-5_5
- Riding, R. (2000) Microbial carbonates: the geological record of calcified bacterial–algal mats and biofilms. *Sedimentology*, 47, 179–214. <https://doi.org/10.1046/j.1365-3091.2000.00003.x>
- Riding, R. (2011) Microbialites, stromatolites, and thrombolites. In: Reitner, J. & Thiel, V. (Eds.) *Encyclopedia of Geobiology*. Springer, Heidelberg: Encyclopedia of Earth Science Series, pp. 635–654. https://doi.org/10.1007/978-1-4020-9212-1_196
- Roberts, A., Kenward, P.A., Fowle, D.A., Goldstein, R.H., González, L.A. & Moore, D.S. (2013) Moore Surface chemistry allows for abiotic precipitation of dolomite at low temperature. *Proceedings of the National Academy of Sciences of the United States of America*, 110, 14540–14545. <https://doi.org/10.1073/pnas.1305403110>
- Roberts, N.M.W., Rasbury, E.T., Parrish, R.R., Smith, C.J., Horstwood, M.S.A. & Condon, D.J. (2017) A calcite reference material for LA-ICP-MS U-Pb geochronology. *Geochemistry, Geophysics, Geosystems*, 18, 2807–2814. <https://doi.org/10.1002/2016GC006784>
- Šajnović, A., Stojanović, K., Jovančević, B. & Cvetković, O. (2008) Biomarker distributions as indicators for the depositional environment of lacustrine sediments in the Valjevo-Mionica basin (Serbia). *Chemie der Erde-Geochemistry*, 68, 395–411.
- Šajnović, A., Grba, N., Neubauer, F., Kašanin-Grubin, M., Stojanović, K., Petković, N. & Jovančević, B. (2020) Geochemistry of sediments from the Lopare Basin (Bosnia and Herzegovina): implications for paleoclimate, paleosalinity, paleoredox and provenance. *Acta Geologica Sinica*, 94, 1591–1618.
- Sant, K., Andrić, N., Mandić, O., Demir, V., Pavelić, D., Rundić, L., Hrvatović, H., Matenco, L. & Krijgsman, W. (2018) Magneto-biostratigraphy and paleoenvironments of the Miocene freshwater sediments of the Sarajevo-Zenica Basin. *Palaeogeography, Palaeoclimatology, Palaeoecology*, 506, 48–69.
- Sant, K., Mandić, O., Rundić, L., Kuiper, K.F. & Krijgsman, W. (2018) Age and evolution of the Serbian Lake System: integrated results from Middle Miocene Lake Popovac. *Newsletters on Stratigraphy*, 51, 117–143.
- Schagerl, M. & Renaut, R.W. (2016) Dipping into the soda lakes of East Africa. In: Schagerl, M. (Ed.) *Soda Lakes of East Africa*. Cham, Switzerland: Springer, pp. 3–24.
- Schefer, S., Cvetković, V., Fügenschuh, B., Kounov, A., Ovtcharova, M., Schaltegger, U. & Schmid, S. (2011) Cenozoic granitoids in the Dinarides of southern Serbia: age of intrusion, isotope geochemistry, exhumation history and significance for the geodynamic evolution of the Balkan Peninsula. *International Journal of Earth Sciences*, 100, 1181–1206.
- Schefer, S., Egli, D., Missoni, S., Bernoulli, D., Fügenschuh, B., Gawlick, H.J., Jovanović, D., Krystyn, L., Lein, R., Schmid, S.M. & Sudar, M.N. (2010) Triassic metasediments in the Internal Dinarides (Kopaonik area, southern Serbia): stratigraphy, paleogeographic and tectonic significance. *Geologica Carpathica*, 61, 89–109.
- Schieber, J., Bose, P.K., Eriksson, P.G., Banerjee, S., Sarkar, S., Altermann, W. & Catuneanu, O. (2007) Atlas of Microbial Mat Features Preserved within the Siliciclastic Rock. *Record*, 2, 324.
- Schlunegger, F., Norton, K.P., Delunel, R., Ehlers, T.A. & Madella, A. (2017) Late Miocene increase in precipitation in the Western

- Cordillera of the Andes between 18–19°S latitudes inferred from shifts in sedimentation patterns. *Earth and Planetary Science Letters*, 462, 157–168. <https://doi.org/10.1016/j.epsl.2017.01.002>
- Schmid, S., Bernoulli, D., Fügenschuh, B., Matenco, L., Schefer, S., Schuster, R., Tischler, M. & Ustaszewski, K. (2008) The Alpine-Carpathian-Dinaridic orogenic system: correlation and evolution of tectonic units. *Swiss Journal of Geosciences*, 101, 139–183.
- Smith, G.I. (1979) Subsurface stratigraphy and geochemistry of late Quaternary evaporites, Searles Lake, California. In: U.S. Geological Survey Professional Paper 1043, 130 pp.
- Smith, G.I. & Medrano, M.D. (1996) Continental borate deposits of Cenozoic age. In: Grew, E.S. & Anovitz, L.M. (Eds.) *Boron: mineralogy, petrology and geochemistry*, Vol. 33. Warehouse, US: USGS Publications, pp. 263–298.
- Smith, M.E., Carroll, A.R. & Scott, J.J. (2015) Stratigraphic expression of climate, tectonism, and geomorphic forcing in an underfilled Lake Basin: Wilkins Peak Member of the Green River Formation. In: Smith, M. & Carroll, A. (Eds.) *Stratigraphy and paleolimnology of the Green River Formation, Western USA*, Syntheses in Limnogeology, Vol. 1. Dordrecht: Springer. https://doi.org/10.1007/978-94-017-9906-5_4
- Steele-MacInnis, M., Bodnar, R.J. & Naden, J. (2011) Numerical model to determine the composition of H₂O–NaCl–CaCl₂ fluid inclusions based on microthermometric and microanalytical data. *Geochimica et Cosmochimica Acta*, 75(1), 21–40.
- Steele-MacInnis, M., Lecumberri-Sanchez, P. & Bodnar, R.J. (2012) HokieFlincs_H₂O–NaCl: a Microsoft excel spreadsheet for interpreting microthermometric data from fluid inclusions based on the PVTX properties of H₂O–NaCl. *Computers & Geosciences*, 49, 334–337.
- Stober, I. & Bucher, K. (2004) Fluid sinks within the earth's crust. *Geofluids*, 4(2), 143–151.
- Stober, I. & Bucher, K. (2005) The upper continental crust, an aquifer and its fluid: hydraulic and chemical data from 4 km depth in fractured crystalline basement rocks at the KTB test site. *Geofluids*, 5(1), 8–19.
- Stojadinović, U., Matenco, L., Andriessen, P.A.M., Toljić, M. & Foeken, J.P.T. (2013) The balance between orogenic building and subsequent extension during the tertiary evolution of the NE Dinarides: constraints from low temperature. *Global and Planetary Change*, 103, 19–38.
- Swihart, G.H., McBay, E.H., Smith, D.H. & Siefke, J.W. (1996) A boron isotopic study of a mineralogically zoned lacustrine borate deposit: the Kramer deposit, California, U.S.A. *Chemical Geology*, 127(1–3), 241–250. [https://doi.org/10.1016/0009-2541\(95\)00094-1](https://doi.org/10.1016/0009-2541(95)00094-1)
- Talling, P.J., Masson, D.G., Sumner, E.J. & Malgesini, G. (2012) Subaqueous sediment density flows: depositional processes and deposit types. *Sedimentology*, 59(7), 1937–2003.
- Tänavsuu-Milkeviciene, K. & Sarg, J.F. (2012) Evolution of an organic-rich lake basin – stratigraphy, climate and tectonics: Piceance Creek basin, Eocene Green River Formation. *Sedimentology*, 59, 1735–1768. <https://doi.org/10.1111/j.1365-3091.2012.01324.x>
- Tanner, L.H. (2002) Borate formation in a perennial lacustrine setting: Miocene–Pliocene Furnace Creek Formation, Death Valley, California, USA. *Sedimentary Geology*, 148(2002), 259–273.
- Urošević, M., Pavlović, Z., Klisić, M., Brković, T., Malešević, M. & Trifunović, S. (1970a) Basic Geological Map of the SFRY, 1:100.000, Sheet Novi Pazar (K34–3), Savezni Geološki Zavod, Beograd (1966).
- Urošević, M., Pavlović, Z., Klisić, M., Brković, T., Malešević, M. & Trifunović, S. (1970b) Basic Geological Map of the SFRY, 1:100.000, Sheet Vrnjci (K34–18), Savezni Geološki Zavod, Beograd (1966).
- Ventura, D., Abels, H.A., Hilgen, F.J. & De Boer, P.L. (2018) Orbital-climate control of mass-flow sedimentation in a Miocene alluvial-fan succession (Teruel Basin, Spain). In: Ventra, D. & Clarke, L.E. (Eds.) *Geology and geomorphology of alluvial and fluvial fans: terrestrial and planetary perspectives*, Vol. 440. Geological Society, London, Special Publications, pp. 129–157. <https://doi.org/10.1144/SP440.14>
- Walter, B.F., Burisch, M. & Markl, G. (2016) Long-term chemical evolution and modification of continental basement brines—a field study from the Schwarzwald, SW Germany. *Geofluids*, 16, 604–623.
- Walter, B.F., Burisch, M., Marks, M.A. & Markl, G. (2017) Major element compositions of fluid inclusions from hydrothermal vein-type deposits record eroded sedimentary units in the Schwarzwald district, SW Germany. *Mineralium Deposita*, 52, 1191–1204.
- Walter, B.F., Gerdes, A., Kleinhanns, I.C., Dunkl, I., von Eynatten, H., Kreissl, S. & Markl, G. (2018) The connection between hydrothermal fluids, mineralization, tectonics and magmatism in a continental rift setting: fluorite Sm–Nd and hematite and carbonates U–Pb geochronology from the Rhinegraben in SW Germany. *Geochimica et Cosmochimica Acta*, 240, 11–42.
- Walter, B.F., Giebel, R.J., Siegfried, P., Doggart, S., Macey, P., Schiebel, D. & Kolb, J. (2023) The genesis of hydrothermal veins in the Aukam valley SW Namibia—a far field consequence of Pangean rifting? *Journal of Geochemical Exploration*, 250, 107229.
- Walter, B.F., Immenhauser, A., Geske, A. & Markl, G. (2015) Exploration of hydrothermal carbonate magnesium isotope signatures as tracers for continental fluid aquifers, Schwarzwald mining district, SW Germany. *Chemical Geology*, 400, 87–105.
- Walter, B.F., Kortenbruck, P., Scharrer, M., Zeitvogel, C., Wälle, M., Mertz-Kraus, R. & Markl, G. (2019) Chemical evolution of ore-forming brines—Basement leaching, metal provenance, and the redox link between barren and ore-bearing hydrothermal veins. A case study from the Schwarzwald mining district in SW-Germany. *Chemical Geology*, 506, 126–148.
- Weller, O.M., Mottram, C.M., St-Onge, M.R., Möller, C., Strachan, R., Rivers, T. & Copley, A. (2021) The metamorphic and magmatic record of collisional orogens. *Nature Reviews Earth and Environment*, 2, 781–799. <https://doi.org/10.1038/s43017-021-00218-z>
- Yang, Z., Whitaker, F.F., Liu, R., Phillips, J.C. & Zhong, D. (2021) A new model for formation of lacustrine primary dolomite by subaqueous hydrothermal venting. *Geophysical Research Letters*, 48, e2020GL091335. <https://doi.org/10.1029/2020GL091335>
- Zachos, J., Pagani, M., Sloan, L., Thomas, E. & Billups, K. (2001) Trends, rhythms, and aberrations in global climate 65 Ma to present. *Science*, 292(5517), 686–693.
- Zhang, Y., Tan, H., Cong, P., Rao, W., Ta, W., Lu, S. & Shi, D. (2022) Boron and lithium isotopic constraints on their origin, evolution, and enrichment processes in a river–groundwater–salt

lake system in the Qaidam Basin, northeastern Tibetan Plateau. *Ore Geology Reviews*, 149, 105110. <https://doi.org/10.1016/j.oregeorev.2022.105110>

Zhao, Z., Zhao, J., Wang, H., Liao, J. & Liu, C. (2007) Distribution characteristics and applications of trace elements in Junggar Basin. *Natural Gas Exploration and Development*, 30, 30–33 (in Chinese with English abstract).

SUPPORTING INFORMATION

Additional supporting information can be found online in the Supporting Information section at the end of this article.

How to cite this article: Andrić-Tomašević, N., Walter, B.F., Simić, V., Raza, M., Životić, D., Novković, Ž. et al. (2025) Contributions of arid climate and hydrothermal fluid flow on sedimentation in saline-alkaline lakes: Insight from the Ibar intramontane basin (Southern Serbia). *The Depositional Record*, 00, 1–34. Available from: <https://doi.org/10.1002/dep2.70017>